Yamamoto N, Kimura H	long-term propagation of rat bone marrow cells.				
Saeng A.S, Wichukchinda N, Myint L, Pathipvanich P, Ariyoshi K, Rojanawiwat A, Matsuda M, Sawanpanyalert P, Sugiura W, Auwanit W	Study of Antiretroviral Drug Resistant HIV-1 Genotypes in Northern Thailand : Role of Mutagenically Separated Polymerase Chain Reaction as a Tool for Monitoring Zidovudine – Resistant HIV-1 in Resource – Limited Settings.	Journal of Acquired Immune Deficiency Syndromes	Vol.36, No.5	1051-1056	2004

Resistant Mechanism against Nelfinavir of Human Immunodeficiency Virus Type 1 Proteases

Hirotaka Ode,* Masami Ota, Saburo Neya, Masayuki Hata, Wataru Sugiura,† and Tyuji Hoshino

Graduate School of Pharmaceutical Sciences, Chiba University, Chiba 263-8522, Japan

Received: July 15, 2004; In Final Form: October 12, 2004

Inhibitors against human immunodeficiency virus type-1 (HIV-1) proteases are finely effective for anti-HIV-1 treatments. However, the therapeutic efficacy is reduced by the rapid emergence of inhibitor-resistant variants of the protease. Among patients who failed in the inhibitor nelfinavir (NFV) treatment, D30N, N88D, and L90M mutations of HIV-1 protease are often observed. Despite the serious clinical problem, it is not clear how these mutations, especially nonactive site mutations N88D and L90M, affect the affinity of NFV or why they cause the resistance to NFV. In this study, we executed molecular dynamics simulations of the NFV-bound proteases in the wild-type and D30N, N88D, D30N/N88D, and L90M mutants. Our simulations clarified the conformational change at the active site of the protease and the change of the affinity with NFV for all of these mutations, even though the 88th and 90th residues are not located in the NFV-bound cavity and not able to directly interact with NFV. D30N mutation causes the disappearance of the hydrogen bond between the *m*-phenol group of NFV and the 30th residue. N88D mutation alters the active site conformation slightly and induces a favorable hydrophobic contact. L90M mutation dramatically changes the conformation at the flap region and leads to an unfavorable distortion of the binding pocket of the protease, although 90M is largely far apart from the flap region. Furthermore, the changes of binding energies of the mutants from the wild-type protease are shown to be correlated with the mutant resistivity previously reported by the phenotypic experiments.

Introduction

Replication of human immunodeficiency virus type 1 (HIV-1) requires the processing of gag and gag-pol polyprotein precursors by the virus-encoded aspartic protease, so-called HIV-1 protease.[1] Therefore, the protease has been one of the major targets of anti-HIV-1 treatments.[2] Today, seven protease inhibitors (PIs) are approved by the FDA and are available clinically. Those drugs are well-designed to fit the inside of the binding cavity, mimicking the configuration of a substrate in the transition state for the hydrolysis reaction by the protease.[3] However, HIV-1 frequently acquires the resistance to these inhibitors through specific mutations due to the high polymorphism and adaptability of the protease.[4−7] Serious resistant mutants survive during the treatment with PIs and cause a failure in long-term HIV chemotherapy.

Among patients who failed in the treatment with nelfinavir, NFV (Figure 1), which is one of the PIs, substitutions of asparagine (N) for aspartic acid (D) at codon 30 (D30N), aspartic acid for asparagine at codon 88 (N88D), and methionine (M) for leucine (L) at codon 90 (L90M) are frequently seen in HIV-1 protease.[8,9] D30N is a primary NFV-resistant mutation, which appears to be very specific for this inhibitor. N88D is an additional mutation to D30N. A combination of D30N and N88D is the most commonly seen in patients treated with NFV, and N88D compensates for the loss of replicative capacity resulting from D30N as a secondary mutation. L90M is a primary mutation responsible for the resistance to both NFV and saquinavir[10] and also appears to be associated with the resistance to the other PIs.[4−6] There are two evolutionarily possible pass ways for the NFV-related mutation acquisition, and the L90M acquisition pass way is evolutionarily different from the pass way of D30N.[11,12]

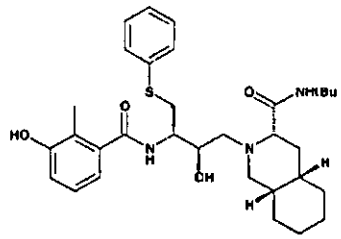

Figure 1. Structure of NFV. According to the crystal structure (PDB code: 1OHR), the *m*-phenol group of the 2-methyl-3-hydroxylbenzamide side chain of NFV interacts with 30D by hydrogen bonding in the S2 pocket of HIV-1 protease. The *tert*-butylcarboxamide moiety occupies the S2′ subsite, the S-phenyl group and dodecahydroisoquinoline ring fit into the hydrophobic S1 and S1′ pockets, and the central hydroxyl group is bound to the catalytic aspartates.

The three-dimensional X-ray structure of the NFV-bound protease[13] implies that D30N mutation would alter the direct electrostatic interaction with the *m*-phenol group of NFV at the active site (Figure 2). It is, however, difficult to understand the NFV resistance due to N88D or L90M mutations because these 88th and 90th residues are located at the nonactive site near the dimer interface. Recently, Mahalingam and co-workers determined some high-resolution X-ray crystal structures of D30N, N88D, or L90M mutants combined with peptide inhibitor analogues, not NFV,[14−16] and suggested the mechanism of the resistance. They found that D30N mutation altered the interac-

* Corresponding author. Tel.: +81-43-290-2926. Fax: +81-43-290-2925. E-mail: odehir@graduate.chiba-u.jp.

† AIDS Research Center, National Institute of Infectious Diseases, Musashimurayama, Tokyo 208-0011, Japan.

10.1021/jp046860+ CCC: $30.25
Published on Web 12/09/2004

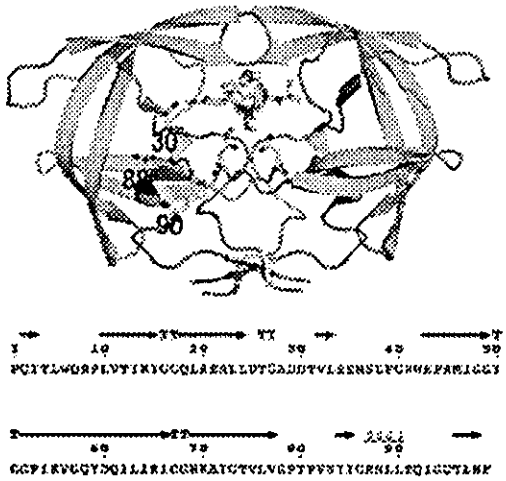

Figure 2. X-ray structure of the HIV-1 protease/NFV complex (PDB code: 1OHR). Locations of the two catalytic aspartates and the residues related with NFV resistance (30, 88, 90) are shown in the stick representation in one subunit of the protease dimer. The wild-type sequence is shown below.

tion with the inhibitors, N88D mutation lost the water that mediated hydrogen bond interactions among 31T, 74T, and 88D, and L90M caused an unfavorable van der Waals contact between 24T/25D and the long side chain of 90M. Further, they reported that L90M mutants altered the active site conformation when indinavir entered the binding cavity of the protease.[17] Though these structural features might be seen in the proteases complexed with NFV, a clear explanation on the resistance to NFV due to these mutations has not been provided yet.

Computational chemistry has been developed in recent years, and detailed analysis has been significantly improved. Many computational works were already carried out to clarify the catalytic mechanism of HIV-1 protease in its substrate-hydrolysis reaction.[18−30] And the other works discussed the drug-resistant mechanisms of some familiar active site mutations.[31−36] In the present study, we discussed the resistant mechanism of not only active site mutation D30N but also nonactive site mutations N88D, L90M. To clarify these mechanisms, we investigated the wild-type HIV-1 protease and D30N, N88D, D30N/N88D, and L90M mutants complexed with NFV on the basis of the molecular dynamics (MD) approach explicitly including the solvate condition. Our MD simulations for each mutant demonstrated the respective resistant mechanisms to NFV. Not only active site mutation D30N but also nonactive site mutations N88D and L90M affect the interaction between NFV and the protease through the structural modification of the binding cavity. There are no papers reported on the resistant mechanism of the nonactive site mutations through a computational approach. The atom-level understanding of the origins of these resistances will be useful in the design of better PIs. Further, our work suggests the possibility to reproduce the experimental phenotype data from the results of MD simulation.

Materials and Methods

MD Simulation. The reliability of MD simulations largely depends on the selection of force field parameters and the assignment of atomic charges. Hence, the electrostatic potential of NFV was preliminarily calculated at the B3LYP/6-31G(d, p) level using the Gaussian 98 program[37] after geometry optimization. The partial atom charges for NFV utilized in the MD simulation were determined using the RESP method[38] so that the atom charges could reproduce the values of the calculated electrostatic potential at the surrounding points of NFV. The charges were set equal between two atoms if they are the same element and have the same bond coordination. Afterward, all the minimizations and MD simulations were executed with the Sander module of AMBER 7 package.[39] The AMBER parm99 force field[40] was used as the parameters for the van der Waals and the bonded energy terms.

Each initial structure for the wild-type protease of clade B and D30N, N88D, D30N/N88D, and L90M mutants complexed with NFV was modeled on the basis of the coordinates of an X-ray crystal structure (PDB code: 1OHR)[13] using the LEaP module. All the crystal waters were included in each model. Each model was placed in a periodic cubic box filled with the about 8000 TIP3P water molecules.[41] The cutoff distance for the long-range electrostatic and the van der Waals terms was 12.0 Å. All covalent bonds to hydrogen atoms were constrained using the SHAKE algorithm.[42] Periodic boundary conditions were applied to avoid the edge effects in all calculations. Energy minimization was achieved via three stages. At first, the movement was allowed only for the water molecules. Next, the ligand and the mutated residues were allowed to move in addition to the water molecules. Last, all atoms were permitted to move freely. In each stage, energy minimization was executed by the steepest decent method for the first 1000 steps and the conjugated gradient method for the subsequent 3000 steps. The protonation states of the catalytic aspartates 25D/25′D were determined performing energy minimizations for all combinations of the protonation states (25D/25′D both protonated, 25D/25′D both unprotonated, 25D protonated and 25′D unprotonated, 25D unprotonated and 25′D protonated). The combination with protonated 25D and unprotonated 25′D showed the lowest total potential energy. This protonation state is consistent with the results of the previous work by Zoete et al.[43]

After 24-ps heating calculations until 300 K using the NVT ensemble, MD simulations were executed using the NPT ensemble at 1 atm and at 300 K for more than 1 ns, with a basic time step of 1 fs. After 500-ps equilibrating calculations, the MD simulations showed no large fluctuations (the deviation of the root-mean square deviation, RMSD, of the main chain is less than 0.1 Å in each model; more detailed data are shown in Supporting Information). Coordinates of 200 snapshots at the intervals of 0.5 ps were obtained as structural data; those were collected for the last 100 ps of the simulations.

Difference Distance Plot. The difference distance plots are drawn to assess the intermolecular relative shifts in response to the mutation. First, $C\alpha_i$-to-$C\alpha_j$ distances, $\mathbf{d}_{ij}^{A}$, are computed for all the combinations of the Cα atoms in the protease of a mutant (A). Second, the same distances, $\mathbf{d}_{ij}^{B}$, are measured for the wild-type model (B). The difference distances $\mathbf{d}_{ij}^{AB}$ of the residues i and j are given by

$$\mathbf{D}_{ij}^{AB} = |\mathbf{d}_{ij}^{A} - \mathbf{d}_{ij}^{B}|$$

Further, the error-scaled difference distance[44,45] $\mathbf{E}_{ij}^{AB}$ is estimated by

$$\mathbf{E}_{ij}^{AB} = \mathbf{D}_{ij}^{AB} / \sigma(\mathbf{D}_{ij}^{AB})$$

$$\sigma(\mathbf{D}_{ij}^{AB}) = [(\sigma_{r,i}^{A})^2 + (\sigma_{r,j}^{A})^2 + (\sigma_{r,i}^{B})^2 + (\sigma_{r,j}^{B})^2]^{1/2}$$

where $\sigma_{r,i}^{\wedge}$ is the radial positional error that corresponds to the uncertainty for an individual atom position. The difference distance is plotted on the lower left panel, and the error-scaled

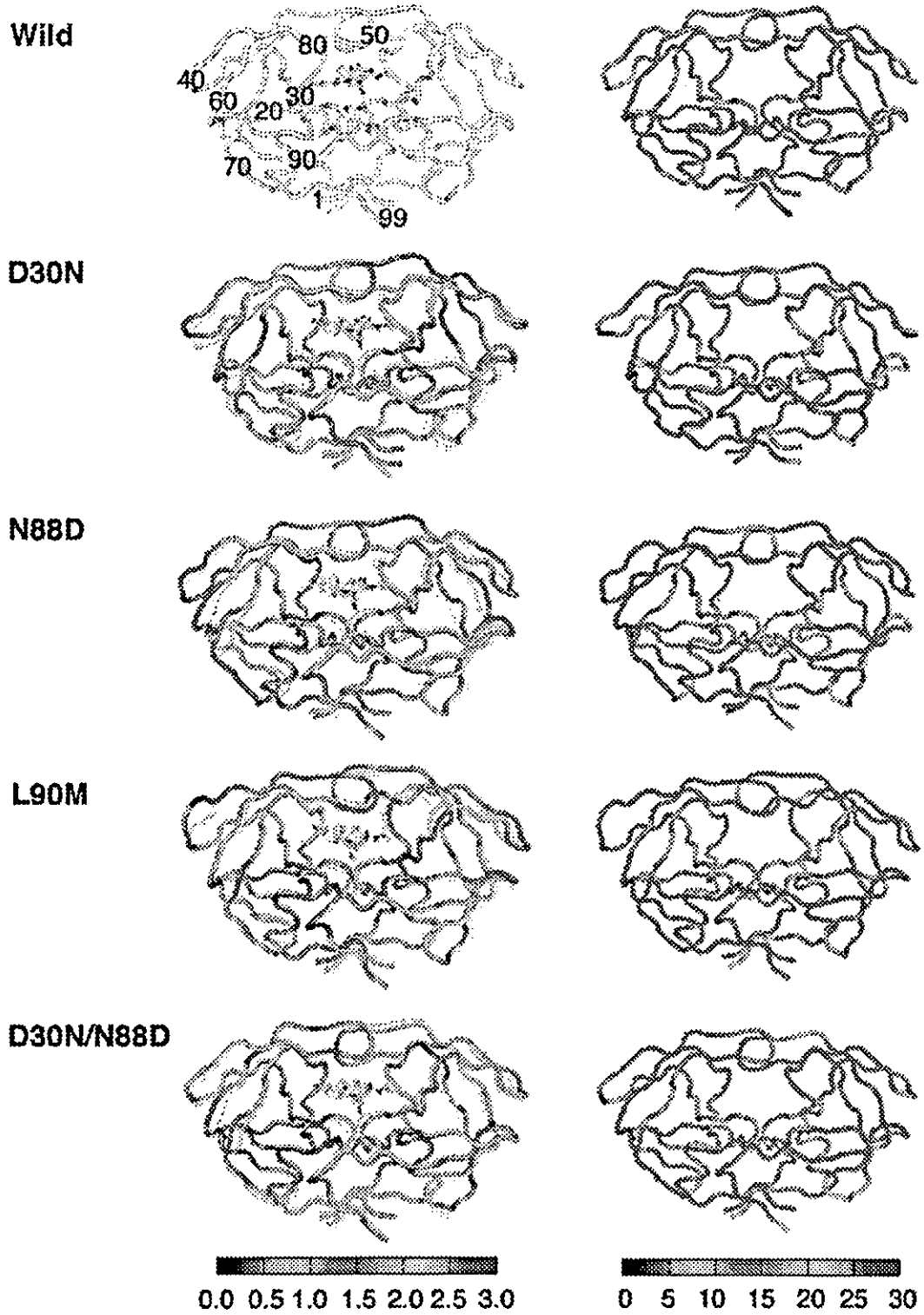

Figure 3. Left: Plots of RMSD between the average structures of the wild-type protease and each mutant, traced over every main chain atom. Each mutant structure is superimposed on the wild-type structure represented by white tubes. Right: B-factor values for main chain atoms in the wild-type and mutated proteases. The color represents the magnitude of the RMSD and B-factor shown at the lower bar. Scales are in units of angstroms and squared angstroms, respectively.

difference distance is on the upper right one in the two-dimensional map of Figure 4 as a function of residue numbers by using GNUPLOT.[46]

Hydrogen Bond Criterion. The formation of a hydrogen bond was defined in terms of distance and orientation. The combination of donor D, hydrogen H, and acceptor A atoms

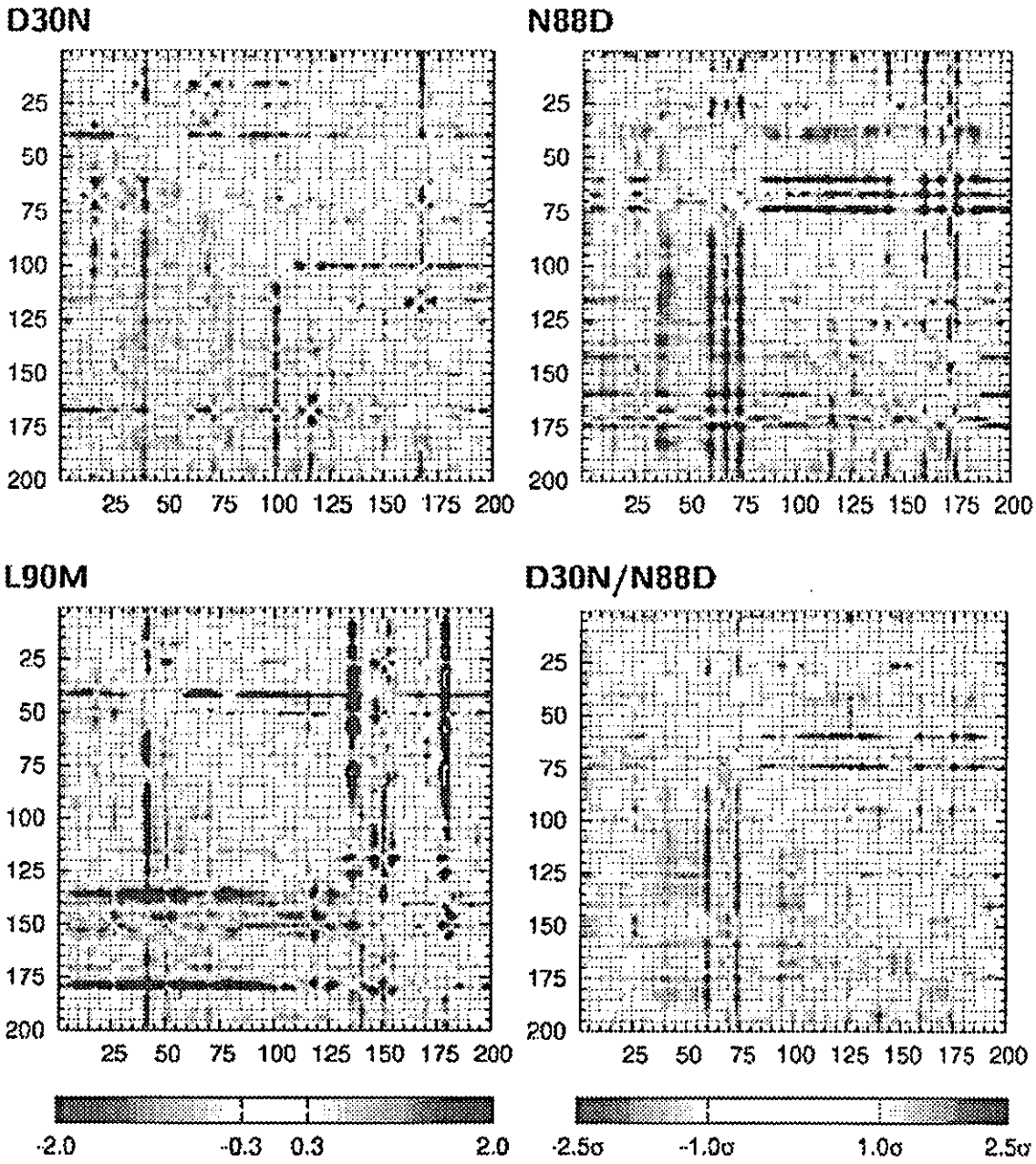

Figure 4. Difference distance matrixes and error-scaled difference matrixes for the Cα atoms. The difference distances for all pairs of residues in the protease are shown on the lower panel. The color represents the magnitude, as shown on the bar on the lower left. The upper right panel shows the error-scaled difference distance matrixes. Changes greater than 1.0σ and smaller than 2.5σ are colored as seen on the lower right bar. Numbers 1−99 represent the residues from 1P to 99F, and numbers 101−199 represents the residues from 1′P to 99′F.

with a D−H···A configuration is regarded as a hydrogen bond when the distance between donor D and acceptor A is shorter than R_{max} and the angle H−D−A is smaller than Θ_{max}. The values of 3.5 Å and 60.0° were adopted for R_{max} and Θ_{max} in this study.

Buried Surface Area (SA). The solvate accessible SA[47] was computed with Paul Beroza's molsurf program, which was based on the analytical technique primarily developed by Connolly[48] to evaluate the surface area buried by a ligand in binding to the enzyme. The SA is computed for the NFV-bound protease structure. SA is also calculated both for only NFV and for the free protease. The difference in SA values between the bound and the unbound cases is defined as the SA buried on complexation.[49]

Binding Energy Calculation. The binding free energy[50] is calculated on the basis of the next equation:

$$\Delta G_b = \Delta G_{MM} + \Delta G_{sol} - T\Delta S$$

where ΔG_b is the binding free energy in solution, ΔG_{MM} is the interaction energy between the ligand and the protein, ΔG_{sol} is the solvation energy, and $-T\Delta S$ is the conformational entropy contribution to the binding. When it is assumed that the entropies are almost the same in magnitude among the mutants, the

difference in entropy is disregarded in the comparison of the binding energy in this study. ΔG_{MM} is calculated from molecular mechanics (MM) interaction energy:

$$\Delta G_{MM} = \Delta G_{int}^{ele} + \Delta G_{int}^{vdw}$$

where ΔG_{int}^{ele} and ΔG_{int}^{vdw} are electrostatic and van der Waals interaction energies between a ligand and a protein. These energies are computed using the same parameter set with the simulation, and no cutoff is applied for the calculation. Solvation energy ΔG_{sol} can be divided into to the two parts:

$$\Delta G_{sol} = \Delta G_{sol}^{ele} + \Delta G_{sol}^{nonpol}$$

The electrostatic contribution to the solvation free energy (ΔG_{sol}^{ele}) is calculated with the Poisson−Boltzmann method using DelPhi program.[51] The hydrophobic contribution to the solvation free energy (ΔG_{sol}^{nonpol}) is determined as a function of the solvent-accessible surface area.[52]

Results

Conformational Changes of the Protease. To study the mechanism of the drug resistance, we compared the averaged atom coordinates of the wild-type with those of each mutant. The least-squared rigid body superposition indicates that no large conformational alteration appears in the shape of the protease for every mutant, as shown in the left column of Figure 3. The RMSD measurement was executed by using the coordinates of backbone atoms N, Cα, and C in the superimposed structures of the wild-type and each mutant. The RMSD values compared with the wild-type model is 0.8 Å in the D30N, 0.9 Å in the N88D, 1.1 Å in the L90M, and 0.6 Å in the D30N/N88D mutant model, averaged over the whole structure. The detailed analysis of individual residues and the comparison of the local structures, however, provided new understanding on the conformational changes due to the mutation. Although large deviations are seen at the residues of the outside loop region, those residues are not minutely examined because their large fluctuations are commonly observed irrelevant to the mutations in B-factor analysis.[43,53] The most characteristic conformational change is detected in the L90M mutant structure. The L90M mutant structure of our study displays significant backbone deviations at the flap regions (43K-58Q, 43′K-58′Q) and at the 79′P loop (78′G-84′I). The RMSD values are 1.6 Å at the flap of one subunit, 2.0 Å at the opposite flap, and 1.9 Å at the 79′P loop. Those values are very large compared with those of the other mutants (0.5 Å/0.6 Å/0.7 Å in D30N, 0.6 Å/0.7 Å/0.7 Å in N88D, and 0.5 Å/0.6 Å/0.5 Å in D30N/N88D). It should be emphasized that, though the 90th residue is not located at the flap nor at the 79′P loop, L90M affects the conformation at those regions. In the N88D mutant structure, peculiar conformational changes occur at the β sheets consisting of 59Y-75V (RMSD: 1.4 Å) and 59′Y-75′V (RMSD: 1.2 Å). Those regions move far away from the helix region (87R-90L/87′R-90′L). The D30N/N88D mutant structure exhibits the similar conformational changes at the same but much narrower regions of those β sheets: 74T/74′T and its vicinity.

To interpret small and more detailed conformational differences, we compared pairwise Cα−Cα distances in the averaged coordinates of each mutant model with those of the wild-type. Each difference distance is shown in the lower left panel of the map in Figure 4, and the upper right panel shows the error-scaled difference distance.[44,45] Figure 4 also indicates that the L90M model has large conformational changes at the flap region (50I/50′I and its vicinity) and at the loop region at 79′P. The N88D and D30N/N88D models alter the conformations at the β sheets (74′T and its vicinity). In addition, these maps provide more detailed comprehension. The flap conformational alteration in the L90M mutant is owing to the approach of 50I to the triads (25D26T27G/25′D26′T27′G) and the detachment of 50′I from the triads. 79′P, 81′P, and some residues at the same loop are far apart from the residues at the opposite subunit. This loop moves outward and also creates a distance from NFV. The mutants other than L90M exhibit the common structural alteration. For example, the distance between the triad and the flap region is slightly changed. The RMSD from the wild-type at the triads in each subunit is 0.8 Å/1.0 Å (D30N), 0.8 Å/1.2 Å (N88D), and 0.8 Å/1.1 Å (D30N/N88D). These deviations are much larger, compared to the RMSD at the flap region. Hence, characteristic distortion in D30N, N88D, and D30N/N88D is mainly caused by the conformational change of the triad.

The above conformational changes were seen in the last 100 ps of simulation. To ensure that these changes were not just from the local fluctuations of MD simulations, we examined the coordinates for the last 500 ps of simulation. The analysis of the last 500 ps of simulation brought us similar results about the conformational changes. L90M had large deviations at the flap (RMSD: 1.5 Å/1.8 Å) and at the 79′P loop (1.7 Å), compared with wild-type structure. The N88D mutation induced the conformational change at the β sheets around 74T/74′T. In N88D, the RMSD values of the β sheets are 1.4 and 1.2 Å in each subunit. And in D30N/N88D, they are both 0.9 Å. Furthermore, the RMSD values at the triads are 0.8 Å/1.1 Å in D30N, 0.7 Å/1.1 Å in N88D, and 0.8 Å/1.1 Å in D30N/N88D.

Hydrophilic Interactions between NFV and the Protease. In protease−ligand interactions, hydrogen bonds play a crucial role in stabilizing the complex. Hydrogen bonds between the protease and NFV in every model are listed in Table 1. Analysis of the protease−NFV hydrogen bonds suggests that mutation has obviously affected the protease−NFV hydrogen bond network. Only a few residues are responsible for the hydrogen bonds with NFV. Hydrogen bond networks consist of 25D/25′D (catalytic aspartates), 50I/50′I, 30D, 29′D, some water molecules, and NFV. The direct interaction between the carboxyl group of 25′D and the central hydroxyl group of NFV is very frequently seen in every model, whereas the protonated aspartate 25D hardly interacts with NFV, except for the L90M model. At the S2 pocket, the main chain of 30D interacts with the *m*-phenol group of NFV. In the wild-type, the main chain of 30D directly interacts with NFV. In each of the N88D and L90M models, one water molecule links 30D and NFV with a hydrogen bond chain although the distance between the donor and the acceptor atoms is elongated. On the other hand, no hydrogen bond is observed in the mutated D30N and D30N/N88D models. D30N mutation causes the disappearance of the hydrogen bond network at the S2 pocket, because those mutants increase the distances with the *m*-phenol group of NFV and cannot keep any water molecule. At the flap region, one water molecule exists in the neighbor of 50I and/or 50′I and NFV in all models. This water intermediates the intramolecular and intermolecular hydrogen bonds, which results in stabilizing the protease−NFV complex. In the wild-type model, the water links the main chain of 50′I with NFV. Further, a direct hydrogen bond between the sulfur atom of NFV and the main chain of 50I is detected and no water molecule mediates the hydrogen bond from 50I. In contrast, the water mediates the hydrogen bond between NFV and both 50I and 50′I in the D30N model. NFV forms a hydrogen bond network with either 50I or 50′I in the other

TABLE 1: Hydrogen Bond Network in Each Model[a]

		hydrogen bond					
		donor			acceptor		occupancy (%)
wild	catalytic domain	O21	−HOL	(NFV)	OD1	(25′D)	91.0
		O21	−HOL	(NFV)	OD2	(25′D)	95.5
		O	−H2	(WAT208)	O21	(NFV)	60.0
		O	−H1	(WAT208)	OD2	(25′D)	61.0
		N22	−HNM	(NFV)	O	(WAT208)	59.5
	S2 pocket	O38	−HO	(NFV)	O	(30D)	90.0
		N	−H	(30D)	O38	(NFV)	64.5
	flap region	N	−H	(50I)	S74	(NFV)	61.0
		O	−H1	(WAT205)	O17	(NFV)	51.5
		N	−H	(50′I)	O	(WAT205)	61.0
D30N	catalytic domain	O21	−HOL	(NFV)	OD2	(25′D)	100.0
		N22	−HNM	(NFV)	O	(WAT210)	85.0
		O	−H1	(WAT210)	O21	(NFV)	52.5
	flap region	O	−H2	(WAT207)	O17	(NFV)	76.5
		O	−H1	(WAT207)	O25	(NFV)	89.0
		N	−H	(50I)	O	(WAT207)	50.5
		N	−H	(50′I)	O	(WAT207)	93.5
	S2′ pocket	N12	−HNC	(NFV)	O	(WAT4757)	94.5
		N	−H	(29′D)	O	(WAT4757)	85.0
		O	−H2	(WAT4757)	OD1	(29′D)	52.5
N88D	catalytic domain	O21	−HOL	(NFV)	OD2	(25′D)	100.0
	S2 pocket	O	−H1	(WAT3880)	O38	(NFV)	59.0
		N	−H	(30D)	O	(WAT3880)	87.5
		O	−H2	(WAT3880)	O	(30D)	97.5
	flap region	O	−H2	(WAT203)	O17	(NFV)	79.5
		O	−H1	(WAT203)	O25	(NFV)	95.0
		N	−H	(50′I)	O	(WAT203)	100.0
D30N/N88D	catalytic domain	O21	−HOL	(NFV)	OD2	(25′D)	96.5
	flap region	O	−H2	(WAT205)	O25	(NFV)	98.5
		O	−H1	(WAT205)	O17	(NFV)	97.5
		N	−H	(50′I)	O	(WAT205)	96.5
L90M	catalytic domain	O21	−HOL	(NFV)	OD2	(25′D)	100.0
		OD2	−HD2	(25D)	O21	(NFV)	90.5
	S2 pocket	O	−H1	(WAT3836)	O38	(NFV)	73.5
		N	−H	(30D)	O	(WAT3836)	90.0
		O	−H2	(WAT3836)	O	(30D)	99.5
	flap region	O	−H2	(WAT205)	O17	(NFV)	96.5
		O	−H1	(WAT205)	O25	(NFV)	97.5
		N	−H	(50I)	O	(WAT205)	90.5
	S2′ pocket	N12	−HNC	(NFV)	O	(WAT4349)	93.5
		N	−H	(29′D)	O	(WAT4349)	74.5
		O	−H2	(WAT4349)	OD1	(29′D)	74.5

[a] The listed donor and acceptor pairs satisfy the criteria for the hydrogen bond over 50.0% of the time during the last 100 ps of simulation. The nomenclature of the atoms is the same as that of 1OHR.

models (L90M, N88D, and D30N/N88D). Both NFV and the water molecule hardly interact with main chain of 50′I in the L90M mutant and with the main chain of 50I in the N88D and D30N/N88D mutants. Hence, each of the N88D and L90M mutations weakens the hydrogen bond networks around 50I and 50′I, respectively. Interestingly, a water molecule mediating a hydrogen bond with 29′D in the S2 pocket is frequently observed in the simulations of D30N and L90M mutants. Another water molecule mediating an intramolecular hydrogen bond in NFV is located near the catalytic aspartates in both the wild-type and the D30N models (WAT208 and WAT207, respectively). In the wild-type model, this water simultaneously mediates the hydrogen bond between 25′D and NFV.

In addition to the NFV−protease interaction at the active site, the N88D mutation modulates the hydrogen bond network at the surroundings of the 88th residues (Figure 5). In the wild-type, the main chain of 88N has a direct hydrogen bond with the main chain of 29D, and the side chain of 88N interacts with the side chain of 31T. Those hydrogen bonds are also observed in the opposite subunit. Further, one water molecule links 88N with 74T (occupancy is 93.5%) and 88′N with 74′T (75.5%). In each of the D30N and L90M, the 88th residues in both

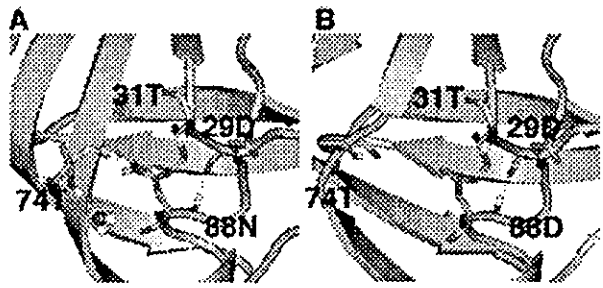

Figure 5. Hydrogen bond network surrounding the 88th residue. A: Wild-type protease structure. B: N88D mutant protease structure.

subunits also have the same hydrogen bond networks as the 29th, 31st, and 74th residues. But in the N88D and D30N/N88D mutant, the water-mediated hydrogen bond does not exist. That is, the N88D mutation induces the disappearance of the hydrogen bonds mediated by water molecules, though the direct hydrogen bonds are retained.

Hydrophobic Interactions between NFV and the Protease. Hydrophobic interactions and van der Waals interactions also contribute to stabilizing the complex. We evaluated the SA

TABLE 2: Buried SA and the Contribution of Hydrophobic and Hydrophilic Residues

	buried SA (Å²)	hydrophobic/hydrophilic[a]
wild	805.9	83.0:17.0
D30N	809.9	82.8:17.2
N88D	841.5	83.1:16.9
D30N/N88D	832.6	86.1:13.9
L90M	765.2	87.1:12.9

[a] Hydrophobic residue: Gly/Ala/Val/Leu/Ile/Met/Pro/Phe/Trp. Hydrophilic residue: Ser/Thr/Asn/Gln/Tyr/Cys/Lys/Arg/His/Asp/Glu.

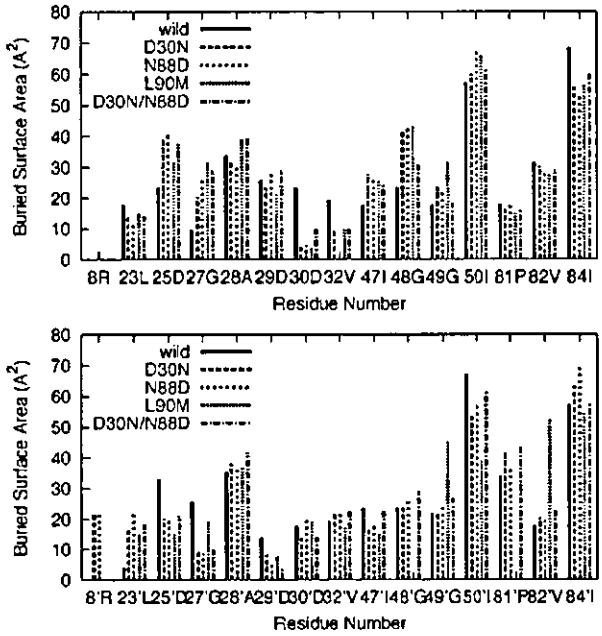

Figure 6. Buried SAs due to each involved residue. The upper graph represents those of one subunit, and the lower graph represents those of the other subunit. L90M shows notable differences at 48′G, 81′P, and 82′V from the other mutants.

buried by the complexation, which is related with the hydrophobicity of the binding cavity and the magnitude of van der Waals contacts between the ligand and the enzyme.[54-56] The results in Table 2 and Figure 6 show that most of the buried residues are hydrophobic ones. The 2-methyl-3-hydroxylbenzamide moiety of NFV has hydrophobic contacts with 23L, 28A, and 84I of the protease at the S2 pocket, and the *tert*-butylcarboxamide moiety has contacts with 32′V and 47′I at the S2′ pocket. Hydrophobic interactions are also seen between the dodecahydroisoquinoline ring and 23L, 28A, 81P, 82V, 84I, and 50′I of the protease at the S1 pocket and between the S-phenyl group and 50I, 23′L, 28′A, 81′P, 82′V, and 84′I at the S1′ pocket. The stabilization caused by hydrophobic interaction is mainly due to 50I/50′I and 84I/84′I, and secondly 28A/28′A, 48G/48′G, and 81′P. The L90M mutant hardly has hydrophobic contacts with NFV at 48′G and 81′P. These little hydrophobic contributions at 48′G and 81′P result in the serious decrease of the buried surface. The D30N mutation hardly affects the buried SA, whereas the N88D mutation increases the buried SA.

Binding Energy Calculation. Table 3 shows the binding energy between NFV and protease. Each mutation causes a distinctive energetic change from the wild-type. D30N decreases the electrostatic energy greatly. N88D becomes more stable because of the electrostatic contribution by the solvation effect than the wild-type. The D30N/N88D model has both characters of D30N and N88D models. D30N/N88D is less stable than N88D because of the electrostatic contribution and is more stable than D30N by the solvation effect. L90M causes a decrease of the electrostatic energy and a large decrease of the van der Waals energy. These energetic results are compatible with the indices of the resistance level that were estimated from experimental IC90.[8,9]

Discussion

We executed MD simulations to understand the resistance mechanism against NFV about not only active site mutation D30N but also N88D and L90M. The simulations suggest that these mutations affect the protease structures on complexation and the NFV−protease interactions, despite the location of the mutated residues.

D30N is a primary mutation of NFV, which emerges during the treatment with this inhibitor highly specifically. The X-ray crystal structure of the wild-type protease complexed with NFV[13] shows that the *m*-phenol group of NFV interacts with both main chain atoms and the side chain carboxyl group of 30D at the S2 pocket. Accordingly, the D30N mutation has been assumed to make less hydrophilic contacts and causes the disappearance of the hydrogen bond interaction from the 30th residue.

Clemente et al. investigated the D30N mutant protease using a docking study previously.[33] They concluded that the D30N mutant would maintain the hydrogen bond between 30N and NFV but weakens the strength of hydrogen bonding due to the decrease of acid−base interaction. However, their computational model could move only NFV and the side chain of 30N in the vacuum condition without any water molecules. That is, their docking simulations did not consider the contributions of the movement of the residues other than 30N nor water solvation effects. MD simulation is useful to incorporate these contributions and to provide more detailed information. The proton or water-mediated hydrogen bonds are observed between the *m*-phenol group of NFV and the main chain of 30D in the wild-type model and the other models having a sequence of 30D, although the side chain carboxyl oxygens of 30D have no hydrogen bonds with NFV. D30N cancels those hydrogen bonds and decreases the electrostatic interaction energy greatly. In addition, we find that the D30N mutation loses its ability to keep any water molecule at the S2 pocket. Then, the substitution of asparagine (N) for aspartate (D) at codon 30 is concluded to

TABLE 3: Binding Free Energies of the Wild-type and Mutants

	ΔG_{int}^{ele} (kcal/mol)	ΔG_{int}^{vdw} (kcal/mol)	ΔG_{sol}^{nonpol} (kcal/mol)	ΔG_{sol}^{ele} (kcal/mol)	$\Delta G_{int+sol}^{ele}$ (kcal/mol)	ΔG_b[a] (kcal/mol)	resistance level[b]
wild	−26.5 ± 4.2	−66.4 ± 3.3	−4.5 ± 0.1	44.2 ± 3.4	17.7 ± 3.5	−53.2 ± 4.2	
D30N	−19.2 ± 2.8	−64.0 ± 2.8	−4.5 ± 0.2	38.2 ± 3.6	19.0 ± 3.7	−49.5 ± 3.5	6
N88D	−26.2 ± 3.5	−66.0 ± 3.5	−4.7 ± 0.3	42.6 ± 3.7	16.4 ± 3.6	−54.3 ± 3.9	0.6
D30N/N88D	−15.1 ± 3.9	−64.9 ± 3.3	−4.6 ± 0.2	35.4 ± 3.7	20.3 ± 3.8	−49.2 ± 4.0	6
L90M	−21.1 ± 3.5	−62.2 ± 3.0	−4.2 ± 0.2	36.4 ± 3.5	15.3 ± 4.0	−51.2 ± 4.0	5

[a] $T\Delta S$ is not included. [b] References 8 and 9.

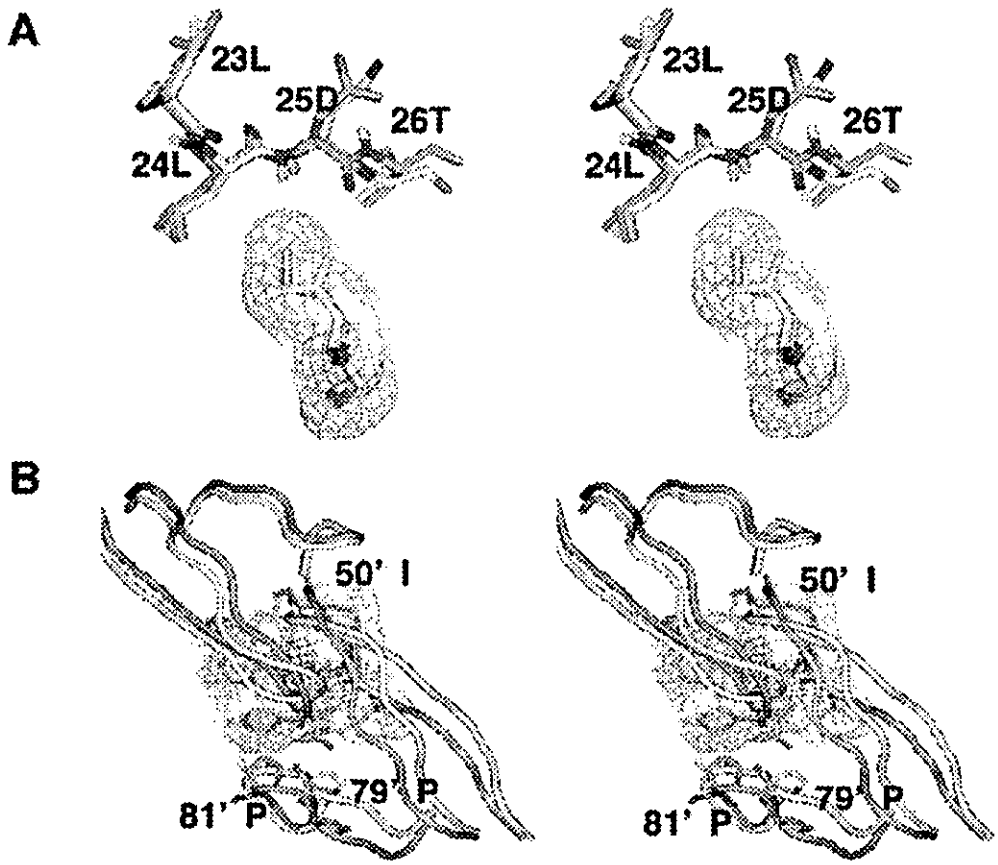

Figure 7. Stereoview of the structures (A) at the surrounding region of the 90th residue and (B) at the flap region. The wild-type structure is represented by white tubes, and L90M mutant is represented by blue tubes.

cause NFV resistance as a result of the serious decrease in the electrostatic interaction.

N88D is known as a secondary mutation for NFV and is frequently seen in the clinical scene next to D30N. Because the 88th residue is located at the helix region near the dimer interface, not at the active site, it is not clear why N88D substitution affects the resistance against NFV. Mahalingam and co-workers determined the X-ray crystal structure of the N88D mutant with substrate analogue inhibitors, not NFV.[14-16] They found that 88N in the wild-type had the proton and/or water-mediated interactions with 29D, 31T, and 74T in each subunit, whereas the corresponding water molecules were missing in both subunits of the N88D single mutant. It is also found from our calculation on the wild-type protease that the side chain of 88N makes a hydrogen bond network with 74T via one water molecule, the backbone nitrogen of 88N has a hydrogen bond with 29D, and the side chain oxygen of 88N interacts with 31T. These hydrogen bond networks are also observed in the opposite subunit. In contrast, in each of the N88D and D30N/N88D mutants, 88D interacts with only 31T and 29D, and the hydrogen bond mediating water molecules disappear in the respective subunit. That is, the 88th residue cannot form any hydrogen bonds with the 74th residue. This disappearance of the water-mediated hydrogen bond allows a large conformational change at the 74th residue. The conformational change at the β sheet consisting of the 74th residue and its adjacent contiguous residues induces the conformational changes at the neighboring β sheet and at the outside loop neighbor to the 74th residue. Further, we have detected that the slight conformational change of the NFV binding pocket due to N88D mutation induces the increase of hydrophobic contacts between NFV and the protease. The loss of the interaction between 74T and 88D would lower the constraint at 29D, 31T, and 74T, which results in the slight conformational change of the active site. Energetic analysis evidently indicates this increase of hydrophobicity. Consequently, NFV is stabilized by the increase of hydrophobic effects when N88D is acquired, while D30N/N88D destabilizes NFV by a large loss of electrostatic interaction. The reduction of the constraint might induce the compensation for the loss of replicative capacity resulting from D30N and keep the binding affinity with substrates, while the resistance against NFV is retained.

90L/M is also located at the helix region near the dimer interface, not at the active site. L90M mutants complexed with a substrate analogue inhibitor, not NFV, were also investigated by Mahalingam and co-workers.[14-16] They concluded that L90M altered van der Waals interactions in the hydrophobic interior at the dimer interface near the catalytic aspartates, and 90L related with the stability of the dimer. We also find the alteration of van der Waals interactions in the L90M model. Side chains of the 90th residues are close to the side chains of 24L/24'L and the main chain of 25D/25'D (Figure 7A). A methionine has a long and straight side chain, while a leucine has a diverging side chain. The substitution of methionine for leucine makes a collision of the 90th residues with 24L/24'L and 25D/25'D. This causes the conformational change at the triads. The conformational change of the triads induces large conformational changes at the flap and at the loop near the 79'P-81'P as a result of the presence of NFV (Figure 7B). Those regions are surprisingly very far apart from the 90th residue. In the L90M

mutant, the conformation in the binding pocket is greatly changed. Specifically, the loop region moves outward from NFV and makes a large gap; therefore, the van der Waals and hydrophobic energies decrease greatly. The character of this conformational change resembles the conformational change of the indinavir-bound L90M protease[17] and the saquinavir-bound G48V/L90M protease.[57] The reason for the multidrug resistance relevant to the L90M mutation would be the conformational change of the triads, and, subsequently, these are hydrophobic at the flap and 79′P loop. The flap and loop region interact with each of the dodecahydroisoquinoline ring of NFV, the pyridyl group of indinavir, and the planar quinoline group of saquinavir. Those chemical bases are the largest in each inhibitor and are very bulky compared with the protease substrates. No structural distortion appears at the loop region of the L90M complexed with the substrate analogue inhibitors. Therefore, it is speculated that the structural distortion seen in the inhibitor-bound L90M mutants is due to the largeness of the quinoline ring or pyridyl group in volume. Then, to reduce or eliminate the resistance of L90M, the moiety that interacts with the loop region should be less bulky.

Our MD studies indicate that the drug-resistant mutations affect the conformations of the binding cavity and the hydrophilic and hydrophobic interactions at the active site, even though the location of mutated residues is apart from the active site.

Furthermore, the difference in the binding energy between the wild-type model and those of each mutant are compatible with the indices of resistance levels that were estimated from experimental IC90.[8,9] At present, there exist some computational approaches to explain the phenotype results.[32,35,58,59] Although each of them successfully predicted the decrease of the binding affinity in the case of the active site mutation, they failed in the prediction of the nonactive site mutation as L90M. Computational prediction is usually based on the assumption that PI resistance is primarily determined by a reduction in binding affinity. Therefore, the previous studies proposed that the drug resistance due to the nonactive site mutation might be caused by another mechanism, such as decreasing the dimer stability of the protease.[57,60] However, our study indicates that the assumption is applicable to the nonactive site mutation. Some nonactive site residues without any direct contact with inhibitors (e.g., 10L, 46M, and 90L) have a strong positional correlation with the residues located at the active site. Hence, the nonactive site mutations would cause a displacement of the active site residues and the decrease of the inhibitor or substrate binding affinity. We suggest that evaluating the positions of all the residues in the mutated protease is a key factor for the success in computational prediction of the protease resistivity against PIs. Additionally, it is also applicable to the design to reduce or to eliminate the resistance at the nonactive site mutations.

Conclusions

We executed MD simulations for the wild-type and D30N, N88D, D30N/N88D, and L90M mutants to clarify the resistant mechanism of each mutation against NFV. Our results could reproduce the phenotype data and clarified the conformational alterations at the active site and the interaction changes due to the mutation. D30N induces the disappearance of the hydrogen bond between the *m*-phenol group of NFV and the 30th residue, which results in the decrease of the electrostatic binding energy. Further, D30N loses the ability to retain a water molecule at the S2 pocket. N88D alters the conformation at the β sheets consisting of 74T and its vicinity greatly. N88D also affects the active site conformation, which creates more favorable hydrophobic binding cavity. L90M affects the triads 25D26T27G and causes subsequent large conformational changes at the flap region and the 79′P loop, though the 90th residue is far apart from those regions. L90M decreases the van der Waals binding energy greatly.

Acknowledgment. This work was supported by the Health and Labor Science Research Grant for Research on HIV/AIDS from Ministry of Health and Labor of Japan.

Supporting Information Available: RMSD of the main chain atoms compared with the X-ray crystal structure (Figure 1S). This material is available free of charge via the Internet at http://pubs.acs.org.

References and Notes

(1) Kohl, N.E.; Emini, E. A.; Schleif, W. A.; Davis, L. J.; Heimbach, J. C.; Dixon, R. A.; Scolnick, E. M.; Sigal, I. S. *Proc. Natl. Acad. Sci. U.S.A.* **1988**, *85*, 4686.

(2) Debouck, C. *AIDS Res. Hum. Retroviruses* **1992**, *8*, 153.

(3) Roberts, N. A.; Martin, J. A.; Kinchington, D.; Broadhurst, A. V.; Craig, J. C.; Duncan, I. B.; Galpin, S. A.; Handa, B. K.; Kay, J.; Krohn, A.; Lambert, R. W.; Merrett, J. H.; Mills, J. S.; Parkes, K. E. B.; Redshaw, S.; Ritchie, A. J.; Taylor, D. L.; Thomas, G. J.; Machin, P. J. *Science* **1990**, *248*, 358.

(4) Johnson, V. A.; Brun-Vézinet, F.; Clotet, B.; Conway, B.; D'Aquila, R. T.; Demeter, L. M.; Kuritzkes, D. R.; Pillay, D.; Schapiro, J. M.; Telenti, A.; Richman, D. *Top. HIV Med.* **2003**, *11*, 215.

(5) Wu, T. D.; Schiffer, C. A.; Gonzales, M. J.; Taylor, J.; Kantor, R.; Chou, S.; Israelski, D.; Zolopa, A. R.; Fessel, W. J.; Shafer, R. W. *J. Virol.* **2003**, *77*, 4836.

(6) Kantor, R.; Fessel, W. J.; Zolopa, A. R.; Israelski, D.; Shulman, N.; Montoya, J. G.; Harbour, M.; Schapiro, J. M.; Shafer, R. W. *Antimicrob. Agents Chemother.* **2002**, *46*, 1086.

(7) Condra, J. H.; Schleif, W. A.; Blahy, O. M.; Gabryelski, L. J.; Graham, D. J.; Quintero, J. C.; Rhodes, A.; Robbins, H. L.; Roth, E.; Shivaprakash, M.; Titus, D.; Yang, T.; Teppler, H.; Squires, K. E.; Deutsch, P. J.; Emini, E. A. *Nature* **1995**, *374*, 569.

(8) Patick, A. K.; Duran, M.; Cao, Y.; Shugarts, D.; Keller, M. R.; Mazabel, E.; Knowles, M.; Chapman, S.; Kuritzkes, D. R.; Markowitz, M. *Antimicrob. Agents Chemother.* **1998**, *42*, 2637.

(9) Patick, A. K.; Mo, H.; Markowitz, M.; Appelt, K.; Wu, B.; Musick, L.; Kalish, V.; Kaldor, S.; Reich, S.; Ho, D.; Webber, S. *Antimicrob. Agents Chemother.* **1996**, *40*, 292 (Erratum, *40*, 1575).

(10) Jacobson, H.; Hängii, M.; Ott, M.; Duncan, I. B.; Owen, S.; Andreoni, M.; Vella, S.; Mous, J. *J. Infect. Dis.* **1996**, *173*, 1379.

(11) Sugiura, W.; Matsuda, Z.; Yokomaku, Y.; Hertogs, K.; Larder, B.; Oishi, T.; Okano, A.; Shiino, T.; Tatsumi, M.; Matsuda, M.; Abumi, H.; Takata, N.; Shirahata, S.; Yamada, K.; Yoshikura, H.; Nagai, Y. *Antimicrob. Agents Chemother.* **2002**, *46*, 708.

(12) Sugiura, W.; Oishi, T.; Okano, A.; Matsuda, M.; Abumi, H.; Yamada, K.; Koike, M.; Taki, M.; Ishikawa, M.; Miura, T.; Hukutake, K.; Gouchi, K.; Ajisawa, A.; Iwamoto, A.; Hanabusa, H.; Mimaya, J.; Takamatsu, J.; Takata, N.; Kakishita, E.; Higasa, S.; Kashiwagi, S.; Shirahata, A.; Nagai, Y. *Jpn. J. Infect. Dis.* **1999**, *52*, 175.

(13) Kaldor, S. W.; Kalish, V. J.; Davies, J. F.; Shetty, B. V.; Fritz, J. E.; Appelt, K.; Burgess, J. A.; Campanale, K. M.; Chirgadze, N. Y.; Clawson, D. K.; Dressman, B. A.; Hatch, S. D.; Khalil, D. A.; Kosa, M. B.; Lubbehusen, P. P.; Muesing, M. A.; Patick, A. K.; Reich, S. H.; Su, K. S.; Tatlock, J. H. *J. Med. Chem.* **1997**, *40*, 3979.

(14) Mahalingam, B.; Boross, P.; Wang, Y.-F.; Louis, J. M.; Fischer, C. C.; Tozser, J.; Harrison, R. W.; Weber, I. T. *Proteins* **2002**, *48*, 107.

(15) Mahalingam, B.; Louis, J. M.; Hung, J.; Harrison, R. W.; Weber, I. T. *Proteins* **2001**, *43*, 455.

(16) Mahalingam, B.; Louis, J. M.; Reed, C. C.; Adomat, J. M.; Krouse, J.; Wang, Y.-F.; Harrison, R. W.; Weber, I. T. *Eur. J. Biochem.* **1999**, *263*, 238.

(17) Mahalingam, B.; Wang, Y.-F.; Boross, P. I.; Tozser, J.; Louis, J. M.; Harrison, R. W.; Weber, I. T. *Eur. J. Biochem.* **2004**, *271*, 1516.

(18) Piana, S.; Bucher, D.; Carloni, P.; Rothlisberger, U. *J. Phys. Chem. B* **2004**, *108*, 11139.

(19) Piana, S.; Parrinello, M.; Carloni, P. *J. Mol. Biol.* **2002**, *319*, 567.

(20) Trylska, J.; Bala, P.; Geller, M.; Grochowski, P. *Biophys. J.* **2002**, *83*, 794.

(21) Okimoto, N.; Kitayama, K.; Hata, M.; Hoshino, T.; Tsuda, M. *THEOCHEM* **2001**, *543*, 53.
(22) Okimoto, N.; Tsukui, T.; Kitayama, K.; Hata, M.; Hoshino, T.; Tsuda, M. *J. Am. Chem. Soc.* **2000**, *122*, 5613.
(23) Park, H.; Suh, J.; Lee, S. *J. Am. Chem. Soc.* **2000**, *122*, 3901.
(24) Okimoto, N.; Tsukui, T.; Hata, M.; Hoshino, T.; Tsuda, M. *J. Am. Chem. Soc.* **1999**, *121*, 7349.
(25) Ventrini, A.; López-Ortiz, F.; Alvarez, J. M.; Gonzalez, J. *J. Am. Chem. Soc.* **1998**, *120*, 1110.
(26) Liu, H.; Müller-Plathe, F.; Van Gusteren, W. F. *J. Mol. Biol.* **1996**, *118*, 3946.
(27) Weber, I. T.; Harrison, R. W. *Protein Eng.* **1996**, *9*, 679.
(28) Harrison, R. W.; Weber, I. T. *Protein Eng.* **1994**, *7*, 1353.
(29) Beveridge, A. J.; Heywood, G. C. *Biochemistry* **1993**, *32*, 3325.
(30) Goldblum, A. *Biochemistry* **1988**, *27*, 1653.
(31) Perryman, A. L.; Lin, J.-H.; McCammon, J. A. *Protein Sci.* **2003**, *13*, 1108.
(32) Shenderovich, M. D.; Kagan, R. M.; Heseltine, P. N. R.; Ramnarayan, K. *Protein Sci.* **2003**, *12*, 1706.
(33) Clemente, J. C.; Hermrajani, R.; Blum, L. E.; Goodenow, M. M.; Dunn, B. M. *Biochemistry* **2003**, *42*, 15029.
(34) Piana, S.; Carloni, P.; Rothlisberger, U. *Protein Sci.* **2002**, *11*, 2393.
(35) Rick, S. W.; Topol, I. A.; Erickson, J. W.; Burt, S. K. *Protein Sci.* **1998**, *8*, 1750.
(36) Harte, W. E., Jr.; Beveridge, D. L. *J. Am. Chem. Soc.* **1993**, *115*, 1231.
(37) Frisch, M. J.; Trucks, G. W.; Schlegel, H. B.; Scuseria, G. E.; Robb, M. A.; Cheeseman, J. R.; Zakrzewski, V. G.; Montgomery, J. A., Jr.; Stratmann, R. E.; Burant, J. C.; Dapprich, S.; Millam, J. M.; Daniels, A. D.; Kudin, K. N.; Strain, M. C.; Farkas, O.; Tomasi, J.; Barone, V.; Cossi, M.; Cammi, R.; Mennucci, B.; Pomelli, C.; Adamo, C.; Clifford, S.; Ochterski, J.; Petersson, G. A.; Ayala, P. Y.; Cui, Q.; Morokuma, K.; Malick, D. K.; Rabuck, A. D.; Raghavachari, K.; Foresman, J. B.; Cioslowski, J.; Ortiz, J. V.; Stefanov, B. B.; Liu, G.; Liashenko, A.; Piskorz, P.; Komaromi, I.; Gomperts, R.; Martin, R. L.; Fox, D. J.; Keith, T.; Al-Laham, M. A.; Peng, C. Y.; Nanayakkara, A.; Gonzalez, C.; Challacombe, M.; Gill, P. M. W.; Johnson, B. G.; Chen, W.; Wong, M. W.; Andres, J. L.; Head-Gordon, M.; Replogle, E. S.; Pople, J. A. *Gaussian 98*; Gaussian, Inc.: Pittsburgh, PA, 1998.
(38) Cieplak, P.; Cornell, W. D.; Bayly, C.; Kollman, P. A. *J. Comput. Chem.* **1995**, *16*, 1357.
(39) Case, D. A.; Pearlman, D. A.; Caldwell, J. W.; Cheatham, T. E., III; Wang, J.; Ross, W. S.; Simmerling, C. L.; Darden, T. A.; Merz, K. M.; Stanton, R. V.; Cheng, A. L.; Vincent, J. J.; Crowley, M.; Tsui, V.; Gohlke, H.; Radmer, R. J.; Duan, Y.; Pitera, J.; Massova, I.; Seibel, G. L.; Singh, U. C.; Weiner, P. K.; Kollman, P. A. *AMBER 7*; University of California: San Francisco, 2002.
(40) Wang, J.; Cieplak, P.; Kollman, P. A. *J. Comput. Chem.* **2000**, *21*, 1049.
(41) Jorgensen, W. L.; Chandrasekhar, J.; Madura, J. D.; Impey, R. W.; Klein, M. L. *J. Chem. Phys.* **1983**, *79*, 926.
(42) Ryckaert, J.-P.; Ciccotti, G.; Berendsen, H. J. C. *J. Comput. Phys.* **1977**, *23*, 327.
(43) Zoete, V.; Michielin, O.; Karplus, M. *J. Mol. Biol.* **2002**, *315*, 21.
(44) Schneider, T. R. *Acta Crystallogr., Sect. D* **2002**, *58*, 195.
(45) Schneider, T. R. *Acta Crystallogr., Sect. D* **2000**, *56*, 714.
(46) Williams, T.; Kelley, C. *GNUPLOT*, 1998 (contact for further information http://www.gnuplot.info/).
(47) Lee, B.; Richards, F. M. *J. Mol. Biol.* **1971**, *55*, 379.
(48) Connolly, M. L. *J. Appl. Crystallogr.* **1983**, *16*, 548.
(49) Prabu-Jeyabalen, M.; Nalivaika, E. A.; King, N. M.; Schiffer, C. A. *J. Virol.* **2003**, *77*, 1306.
(50) Kollman, P. *Chem. Rev.* **1993**, *93*, 2395.
(51) Honig, B.; Nicholls, A. *Science* **1995**, *268*, 1144.
(52) Sitkoff, D.; Sharp, K. A.; Honig, B. *J. Phys. Chem.* **1994**, *98*, 1978.
(53) Karplus, M.; Petsko, G. A. *Nature* **1990**, *347*, 631.
(54) Kuhn, L. A.; Siani, M. A.; Pique, M. E.; Fisher, C. L.; Getzoff, E. D.; Tainer, J. A. *J. Mol. Biol.* **1992**, *228*, 13.
(55) Chothia, C. *J. Mol. Biol.* **1976**, *105*, 1.
(56) Nozaki, Y.; Tanford, C. *J. Biol. Chem.* **1971**, *7*, 2211.
(57) Hong, L.; Zhang, X. C.; Hartsuck, J. A.; Tang, J. *Protein Sci.* **2000**, *9*, 1898.
(58) Jenwitheesuk, E.; Samudrala, R. *BMC Struct. Biol.* **2002**, *3*, 2.
(59) Wang, W.; Kollman, P. A. *Proc. Natl. Acad. Sci. U.S.A.* **2001**, *98*, 14937.
(60) Xie, D.; Gulnik, S.; Gustchina, E.; Yu, B.; Shao, W.; Qoronfleh, W.; Nathan, A.; Erickson, J. W. *Protein Sci.* **1999**, *8*, 1702.

J. Antibiot. 58(1): 65–68, 2005

NOTE

THE JOURNAL OF ANTIBIOTICS

Fungal Phenalenones Inhibit HIV-1 Integrase

Kazuro Shiomi, Ryosuke Matsui, Miki Isozaki, Harumi Chiba, Takahiro Sugai, Yuichi Yamaguchi, Rokuro Masuma, Hiroshi Tomoda, Tomoko Chiba, Hua Yan, Yoshihiro Kitamura, Wataru Sugiura, Satoshi Ōmura, Haruo Tanaka

Received: September 7, 2004 / Accepted: November 27, 2004

Abstract A phenalenone compound, atrovenetinone methyl acetal, was isolated from a culture broth of *Penicillium* sp. FKI-1463 as an HIV-1 integrase inhibitor, and it showed anti-HIV activity *in vitro*. HIV-1 integrase inhibition and anti-HIV activity of two other natural phenalenones were also studied. Among the tested compounds, funalenone inhibited HIV-1 integrase with an IC_{50} value of 10 μM and showed the best selectivity (anti-HIV, IC_{50}=1.7 μM; cytotoxicity, IC_{50}=87 μM).

Keywords: enzyme inhibitor, HIV interase, AIDS, phenalenone

Combined therapeutic regimens with reverse transcriptase inhibitors and protease inhibitors lead to a suppression of human immunodeficiency virus-1 (HIV-1) replication, reduction of viral load, and decline in morbidity and mortality [1, 2]. However, the therapy sometimes fails due to the emergence of mutant viruses that are resistant to these drugs [3]. Thus, it is critical to discover more effective and less toxic anti-HIV agents with different molecular targets in the viral replication cycle. We have previously screened microbial metabolites for new anti-HIV antibiotics that inhibit entry of HIV-1 into the susceptive cells, and found isochromophilones and chloropeptins by a gp120-sCD4 binding assay [4, 5] and actinohivin by a syncytium formation assay [6]. There are three viral enzymes essential for HIV-1 replication, reverse transcriptase, protease, and integrase. Of these, only integrase has not been the target of a clinically used inhibitor. HIV DNA is inserted into the host genome by a specialized DNA recombination reaction in which the viral integrase is the key player [7, 8]. The integration reaction is composed of three steps, 3′-processing, strand transfer, and gap filling, and integrase catalyses the first and second steps. The third step is thought to be catalyzed by cellular enzymes. Many natural and synthetic integrase inhibitors have been reported [8~12] but only a few compounds show high selectivity. Therefore, we screened microbial metabolites for HIV-1 integrase inhibitors, and found that a culture broth of *Penicillium* sp. FKI-1463 has the inhibitory

H. Tanaka (Corresponding author), **K. Shiomi, R. Matsui, M. Isozaki, H. Chiba, T. Sugai:** School of Pharmaceutical Sciences Kitasato University, 5-9-1 Shirokane, Minato-ku, Tokyo 108-8641, Japan, E-mail: tanakah@pharm.kitasato-u.ac.jp

Y. Yamaguchi, R. Masuma, H. Tomoda, S. Ōmura: The Kitasato Institute, 5-9-1 Shirokane, Minato-ku, Tokyo 108-8641, Japan

R. Masuma, H. Tomoda, S. Ōmura: Kitasato Institute for Life Sciences, Kitasato University, 5-9-1 Shirokane, Minato-ku, Tokyo 108-8641, Japan

T. Chiba, H. Yan, W. Sugiura: AIDS Research Center, National Institute of Infectious Diseases, 4-7-1 Gakuen, Musashimurayama-shi, Tokyo 208-0011, Japan

Y. Kitamura: Advanced Clinical Research Center, Institute of Medical Science, The University of Tokyo, 4-6-1 Shirokanedai, Minato-ku, Tokyo 108-8639, Japan

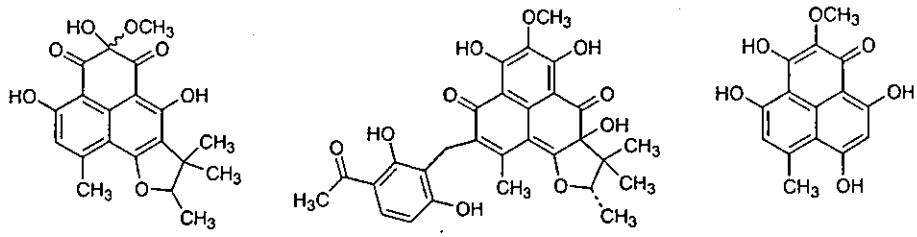

Atrovenetinone methyl acetal (**1**) Erabulenol B (**4**) Funalenone (5)

Fig. 1 Natural phenalenones.

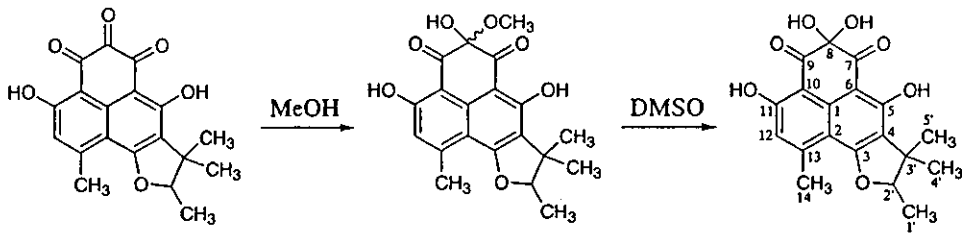

2 **1** **3**

Fig. 2 Conversion of atrovenetinone.

activity. The active compound was identified as a phenalenone compound, atrovenetinone methyl acetal (**1**, Fig. 1) [13]. This paper presents integrase-inhibiting and anti-HIV activities of **1** and other natural phenalenones.

A slant culture of the strain FKI-1463 grown on YpSs agar was inoculated into a 500-ml Erlenmeyer flask containing 100 ml of a seed medium consisting of glucose 2.0%, Polypepton (Nihon Pharmaceutical Co.) 0.5%, yeast extract 0.2% (Oriental Yeast Co.), KH_2PO_4 0.1%, $MgSO_4 \cdot 7H_2O$ 0.05%, and agar 0.1%, pH 6.0. It was cultured on a reciprocal shaker at 27°C for 3 days. One milliliter of the seed culture was transferred into each of twenty 500-ml Erlenmeyer flasks containing 100 ml of a production medium consisting of glycerol 3.0%, oatmeal (Nihon Shokuhin Seizo Co.) 2.0%, dry yeast (Gist-brocades) 1.0%, KH_2PO_4 1.0%, Na_2HPO_4 1.0%, $MgSO_4 \cdot 7H_2O$ 0.5%, pH not adjusted. The fermentation was carried out on a reciprocal shaker at 27°C for 7 days. The cultured broth (2.0 liters) was centrifuged and the mycelia were extracted with methanol, which was then removed from the extract by evaporation. The aqueous extract was partitioned with ethyl acetate at pH 3.0, and the organic layer was concentrated to dryness *in vacuo* to afford brown oil (644 mg). This was chromatographed over a silica gel column. Active fractions, eluted with $CHCl_3$-methanol (100 : 1) and $CHCl_3$-methanol (20 : 1), were concentrated to yield a crude material (284 mg). It was applied on a ODS silica gel column and eluted with aqueous CH_3CN. The 50% CH_3CN eluates were concentrated (95.5 mg) and chromatographed over Sephadex LH-20 to yield green oil (86.8 mg). It was further purified by reverse phase (Pegasil ODS, Senshu Scientific Co.) and normal phase (Pegasil Silica, Senshu Scientific Co.) HPLC to yield 50.5 mg of green oil.

The purified compound was implicated as **1** by comparison of the NMR data in $CDCl_3$ with the reported data by Nakanishi *et al.* [13]. Atrovenetinone (**2**) is easily converted into an acetal in alcohol (Fig. 2) [14], and the acetal is a mixture of diastereomers [13]. So, the NMR spectra of **1** are complicated. Since **2** exists as the hydrate (**3**) in DMSO [14], we observed the NMR spectra of the isolated compound in DMSO-d_6. The spectra were simplified, and each signal was assigned as follows: ^{1}H NMR (600 MHz) δ 13.67 (1H, s, 5-OH), 12.92 (1H, s, 11-OH), 6.86 (1H, s, 12-H), 4.70 (1H, q, J=6.5 Hz, 2′-H), 4.04 (1H, br s, 8-OH), 2.72 (3H, s, 14-H_3), 1.45 (3H, s, 5′-H_3), 1.22 (3H, s, 4′-H_3), 1.41 (3H, d, J=6.5 Hz, 1′-H_3); ^{13}C NMR (150 MHz) δ 197.7 (C-7), 196.2 (C-9), 165.1 (C-11), 164.8 (C-3), 164.5 (C-5), 147.9 (C-13), 136.7 (C-1), 118.1 (C-4), 117.6 (C-12), 109.0 (C-2), 104.9 (C-10), 101.9 (C-6), 91.1 (C-2′), 88.0 (C-8), 42.8 (C-3′), 25.2 (C-5′), 23.5 (C-14), 20.4 (C-4′), 14.3 (C-1′). The NMR data suggested that **1** was converted into **3** in DMSO solution (Fig. 2), and released methanol signals (δ_H 3.15 and δ_C 48.6) were also

Table 1 Biological activities of phenalenones

	IC_{50} (μM)			Selectivity (B/A)
	HIV-1 integrase inhibition	Anti-HIV activity (A)	Cytotoxicity (HPB-M(a)*) (B)	
Atrovenetinone methyl acetal (1)	19	6.7	13	1.9
Erabulenol B (4)	7.9	17	230	14
Funalenone (5)	10	1.7	87	51

*HPB-M(a) cells are human peripheral blood cells transformed by murine leukemia virus. Anti-HIV activity was measured using HPB-M(a) cells with LTR driven luciferase.

observed. Thus, the isolated compound was identified as **1**. It has been reported as a myosin light chain kinase inhibitor isolated from a culture broth of *Penicillium* sp. It may be derived from **2** during purification. Compound **2** is a phenalenone compound originally obtained by the oxidation of atrovenetin produced by *Penicillium* sp., and **2** was lately isolated from a culture broth of *Gremmeniella abietina* [14, 15].

We have previously isolated the other fungal phenalenones, erabulenol B (**4**) which inhibits cholesteryl ester transfer protein and funalenone (**5**) which inhibits collagenase [16, 17]. Funalenone was also reported to inhibit bacterial cell wall synthesis enzymes MraY and MurG [18]. We evaluated integrase inhibition and anti-HIV activity of **1** together with those phenalenones. HIV-1 integrase activity was measured by strand transfer assay according to Craigie *et al.* [7]. *In vitro* anti-HIV activities of the test compounds were measured by originally established reporter human T cell line with LTR driven luciferase. The cells were infected with wild type HIV-1, and the compounds were added at different concentrations ranging from 0.0016 to 125 μg/ml. Luciferase activities of the cells, which appeared to correlate with the level of HIV-1 replication, were measured at day 7, and anti-HIV IC_{50}s of the compounds were evaluated. The IC_{50} value of **1** against integrase was 19 μM, and it also showed anti-HIV activity at 6.7 μM (Table 1). However, its cytotoxicity was relatively high. Compounds **4** and **5** showed more potent inhibition against integrase than **1**, and also exhibited anti-HIV activity. The anti-HIV activity of **5** was the most potent (1.7 μM), and its cytotoxicity (87 μM) was lower than **1**. Though **5** was reported to inhibit collagenase and bacterial cell wall synthesis enzymes [17, 18], those inhibitions were less potent than the integrase inhibition and anti-HIV activity. Therefore, **5** may be a good candidate lead compound for anti-HIV agent. Inhibition of DNA polymerases by the other phenalenones have been reported, but they did not inhibit HIV reverse transcriptase [19]. A plant metabolite, hypericin [20], is the only *ortho*- and *peri*-fused aromatic compound reported to show integrase inhibition [21].

Acknowledgements We are grateful to Dr. Junji Inokoshi, School of Pharmaceutical Sciences, Kitasato University for providing funalenone. This work was supported in part by the Grant of Research for the Development of Anti-AIDS Pharmaceutical Products (KA12505), Japan Health Sciences Foundation, and the 21st Century COE Program, Ministry of Education, Culture, Sports, Science, and Technology.

References

1. Hogg RS, Rhone SA, Yip B, Sherlock C, Conway B, Schechter MT, O'Shaughnessy MV, Montaner JSG. Antiviral effect of double and triple drug combinations amongst HIV-infected adults: lessons from the implementation of viral load-driven antiretroviral therapy. AIDS 12: 279–284 (1998)
2. Palella FJ Jr, Delaney KM, Moorman AC, Loveless MO, Fuhrer J, Satten GA, Aschman DJ, Holmberg SD. Declining morbidity and mortality among patients with advanced human immunodeficiency virus infection. N Engl J Med 338: 853–860 (1998)
3. Deeks SG. Treatment of antiretroviral-drug-resistant HIV-1 infection. Lancet 362: 2002–2011 (2003)
4. Matsuzaki K, Ikeda H, Masuma R, Tanaka H, Ōmura S. Isochromophilones I and II, novel inhibitors against gp120-CD4 binding produced by *Penicillium multicolor* FO-2338. I. Screening, taxonomy, fermentation, isolation and biological activity. J Antibiot 48: 703–707 (1995)
5. Tanaka H, Matsuzaki K, Nakashima H, Ogino T, Matsumoto

A, Ikeda H, Woodruff HB, Ōmura S. Chloropeptins, new anti-HIV antibiotics inhibiting gp120-CD4 binding from *Streptomyces* sp. 1. Taxonomy, fermentation, isolation, physico-chemical properties and biological activities. J Antibiot 50: 58–65 (1997)

6. Chiba H, Inokoshi J, Okamoto M, Asanuma S, Matsuzaki K, Iwama M, Mizumoto K, Tanaka H, Oheda M, Fujita K, Nakashima H, Shinose M, Takahashi Y, Ōmura S. Actinohivin, a novel anti-HIV protein from an actinomycete that inhibits syncytium formation: isolation, characterization, and biological activities. Biochem Biophys Res Commun 282: 595–601 (2001)
7. Craigie R, Hickman AB, Engelman A. Integrase. *In* HIV. Volume 2. *Ed.*, Karn J, pp. 53–71, IRL Press, Oxford (1995)
8. Pommier Y, Neamati N. Inhibitors of human immunodeficiency virus integrase. *In* Advances in Virus Research. Volume 52. *Ed.*, Maramorosch K *et al.*, pp. 427–458, Academic Press, San Diego (1999)
9. Cos P, Maes L, Vanden Berghe D, Hermans N, Pieters L, Vlietinck A. Plant substances as anti-HIV agents selected according to their putative mechanism of action. J Nat Prod 67: 284–293 (2004)
10. Hazuda D, Blau CU, Felock P, Hastings J, Pramanik B, Wolfe A, Bushman F, Farnet C, Goetz M, Williams M, Silverman K, Lingham R, Singh S. Isolation and characterization of novel human immunodeficiency virus integrase inhibitors from fungal metabolites. Antivir Chem Chemother 10: 63–70 (1999)
11. Singh SB, Jayasuriya H, Dewey R, Polishook JD, Dombrowski AW, Zink DL, Guan Z, Collado J, Platas G, Pelaez F, Felock PJ, Hazuda DJ. Isolation, structure, and HIV-1 integrase inhibitory activity of structurally diverse fungal metabolites. J Ind Microbiol Biotechnol 30: 721–731 (2003)
12. Ondeyka JG, Zink DL, Dombrowski AW, Polishook JD, Felock PJ, Hazuda DJ, Singh SB. Isolation, structure and HIV-1 integrase inhibitory activity of exophillic acid, a novel fungal metabolite from *Exophiala pisciphila*. J Antibiot 56: 1018–1023 (2003)
13. Nakanishi S, Toki S, Saitoh Y, Tsukuda E, Kawahara K, Ando K, Matsuda Y. Isolation of myosin light chain kinase inhibitors from microorganisms: dehydroaltenusin, altenusin, atrovenetinone, and cyclooctasulfur. Biosci Biotechnol Biochem 59: 1333–1335 (1995)
14. Ayer WA, Hoyano Y, Pedras MS, van Altena I. Metabolites produced by the Scleroderris canker fungus, *Gremmeniella abietina*. Part 1. Can Chem 64: 1585–1589 (1986)
15. Narasimhachari N, Vining LC. Studies on the pigments of *Penicillium herquei*. Can J Chem 41: 641–648 (1963)
16. Tomoda H, Tabata N, Masuma R, Si SY, Ōmura S. Erabulenols, inhibitors of cholesteryl ester transfer protein produced by *Penicillium* sp. FO-5637. I. Production, isolation and biological properties. J Antibiot 51: 618–623 (1998)
17. Inokoshi J, Shiomi K, Masuma R, Tanaka H, Yamada H, Ōmura S. Funalenone, a novel collagenase inhibitor produced by *Aspergillus niger*. J Antibiot 52: 1095–1100 (1999)
18. Zawadzke LE, Wu P, Cook L, Fan L, Casperson M, Kishnani M, Calambur D, Hofstead SJ, Padmanabha R. Targeting the MraY and MurG bacterial enzymes for antimicrobial therapeutic intervention. Anal Biochem 314: 243–252 (2003)
19. Perpelescu M, Kobayashi J, Furuta M, Ito Y, Izuta S, Takemura M, Suzuki M, Yoshida S. Novel phenalenone derivatives from a marine-derived fungus exhibit distinct inhibition spectra against eukaryotic DNA polymerases. Biochemistry 41: 7610–7616 (2002)
20. Pace N, Mackinney G. Hypericin, the photodynamic pigment from St. John'swort. J Am Chem Soc 63: 2570–2574 (1941)
21. Farnet CM, Wang B, Hansen M, Lipford JR, Zalkow L, Robinson WE, Jr, Siegel J, Bushman F. Human immunodeficiency virus type 1 cDNA integration: new aromatic hydroxylated inhibitors and studies of the inhibition mechanism. Antimicrob Agents Chemother 42: 2245–2253 (1998)

Antiviral Therapy 9:929–935

Influence of single-nucleotide polymorphisms in the multidrug resistance-1 gene on the cellular export of nelfinavir and its clinical implication for highly active antiretroviral therapy

*Dayong Zhu[1], Hitomi Taguchi-Nakamura[1], Mieko Goto[1], Takashi Odawara[2], Tetsuya Nakamura[2], Harumi Yamada[3], Hajime Kotaki[3], Wataru Sugiura[4], Aikichi Iwamoto[1,2] and Yoshihiro Kitamura[1]**

[1]Division of Infectious Diseases, Advanced Clinical Research Centre, Institute of Medical Science, University of Tokyo, Tokyo, Japan
[2]Department of Infectious Diseases and Applied Immunology, Institute of Medical Science, University of Tokyo, Tokyo, Japan
[3]Department of Pharmacy, Research Hospital, Institute of Medical Science, University of Tokyo, Tokyo, Japan
[4]National Institute of Infectious Diseases, Tokyo, Japan

*Corresponding author: +81 3 5449 5336; Fax: +81 3 5449 5427; E-mail: yochan@ims.u-tokyo.ac.jp

Protease inhibitors (PIs) such as nelfinavir (NFV) suppress HIV replication. PIs are substrates of P-glycoprotein (P-gp), the product of the multidrug-resistance-1 (*MDR1*) gene. Three single-nucleotide polymorphisms (SNPs) are present in exons of the *MDR1* gene: *MDR1* 1236, *MDR1* 2677 and *MDR1* 3435. We speculated that these genetic polymorphisms affected PI concentration in the cell. To verify this hypothesis, we first genotyped these SNPs in 79 Japanese patients by the SNaPshot method and found incomplete linkage disequilibrium between the SNPs. Because the SNP at *MDR1* 3435 has been reported to be associated with P-gp expression, we evaluated the effect of that SNP on the export of NFV from HIV-positive patients' lymphoblastoid cell lines by measuring time-dependent decrease in the amount of intracellular NFV by high-performance liquid chromatography. We found the intracellular concentration of NFV in lymphoblastoid cell lines (LCLs) with the homozygous T/T genotype at *MDR1* 3435 were higher than that with C/C genotype with statistical significance. This suggests that the activity of P-gp in patients' LCL cells with the *MDR1* 3435 T/T genotype was lower. In a retrospective study we evaluated the effect of the SNPs on CD4 cell count recovery in response to antiretroviral treatment with PIs, and obtained statistically significant evidence that suggested marginal association of the SNP at *MDR1* 1236 but not at *MDR1* 2677 or *MDR1* 3435. As *in vitro* results were not consistent with the clinical evaluation, clinical importance of *MDR1* genotyping for antiretroviral therapy remains to be investigated in a larger, case-controlled study.

Introduction

Antiretroviral therapy with HIV protease inhibitors (PIs) in combination with reverse transcriptase inhibitors dramatically improved the prognosis of patients infected with HIV-1. However, some patients fail to achieve the maximal virological suppression. We speculate that such failure is partly because PIs do not accumulate in lymphocytes in their active free forms in a concentration high enough to inhibit viral replication [1,2], although the intracellular active PI levels have, to the best of our knowledge, not yet been determined. The activity of P-glycoprotein (P-gp), the product of the multidrug resistance-1 (*MDR1*) gene, appears to affect intracellular PI concentration, because PIs such as nelfinavir (NFV) are substrates of P-gp [2]. P-gp is a glycosylated membrane protein belonging to the ATP-binding cassette superfamily of membrane transporters. P-gp is expressed in many tissues and cell types including intestinal epithelial cells and lymphocytes, where it acts as an energy-dependent exporter [3–9]. The *MDR1* is polymorphic and at least three single-nucleotide polymorphisms (SNPs) have been identified in the exons in a healthy Japanese population [10] as well as in other ethnic groups [6]. *MDR1* 1236 and *MDR1* 3435 are silent mutations in exons 12 and 26 [3,11], respectively, whereas *MDR1* 2677 is a substitution mutation in exon 21 [11]. Reportedly, the SNP at *MDR1* 3435 is associated with the amount and activity of P-gp protein both *in vitro* and *in vivo* [3,12]. In addition, individuals with the T/T genotype at *MDR1* 3435 were found to express less P-gp in lymphocytes and in intestinal epithelial cells [3,13] and showed lower efflux of rhodamine from natural killer (NK)

cells than those with the C/C genotype [13]. According to these observations, *MDR1* polymorphisms seem to affect the intracellular PI concentration and the outcome of antiretroviral treatment. However, the role of *MDR1* 3435 SNP in the response to antiretroviral therapy is still controversial [12,14].

The objective of this study was to evaluate the effect of three *MDR1* SNPs on the intracellular concentrations of NFV and to evaluate the impact of those SNPs on virological and immunological response to antiretroviral treatment, including NFV and PIs. We genotyped the SNPs in 79 Japanese patients and compared the velocity of NFV efflux among selected patients' lymphoblastoid cell lines (LCLs) with different *MDR1* 3435 genotypes. We also analysed the viral loads and CD4 cell counts after initiation of antiretroviral treatment with prescriptions with PIs including NFV in 21 patients.

Materials and methods

Patients

A total of 79 HIV-positive Japanese patients were enrolled in this study. These patients attended a hospital AIDS clinic at the Institute of Medical Science, University of Tokyo (IMSUT). The patients provided their written informed consent to participate in the study and to supply blood samples for DNA analysis and cell culture. Of the 79 patients, 21 receiving highly active antiretroviral therapy (HAART) including PIs were divided into three groups: 11 patients receiving HAART with NFV, four patients receiving HAART with indinavir (IDV) and six patients receiving HAART with saquinavir (SQV) or lopinavir/ritonavir (LPV/RTV). CD4 cell counts and HIV-RNA of plasma were analysed for 9 months after the initiation of the antiretroviral treatment. The study has been approved by the ethics committee of IMSUT.

Single-nucleotide polymorphisms

We typed three single-nucleotide polymorphisms (SNPs) at *MDR1* 1236 (exon 12), *MDR1* 2677 (exon 21) and *MDR1* 3435 (exon 26) by polymerase chain reaction (PCR) followed by ABI PRISM SNaPshot Multiplex Kit (PE Biosystems, Foster City, Calif., USA) [15]. Information on primers and conditions for PCR was obtained at http://snp.ims.u-tokyo.ac.jp [10].

Cells and determination of uptake and efflux of NFV

Peripheral blood mononuclear cells (PBMCs) were separated from patients' whole blood with Ficoll-Conray gradient centrifugation. LCLs were obtained by transforming PBMCs with Epstein-Barr virus (EBV), which was obtained from cell-free supernatants of EBV-producing B95–8 cell lines [16]. LCLs were maintained in RPMI 1640 medium (Sigma-Aldrich, St. Louis, Mo., USA) supplemented with 10% heat-inactivated fetal calf serum.

To determine the time course of NFV uptake into LCL cells, LCL cells (1×10^6/10 ml, counted with a haematocytometer) were incubated at 37°C in a medium containing 10 μM NFV. Cells were harvested by centrifugation at 1500 ×*g* for 5 min at 4°C and immediately frozen at –80°C until high-performance liquid chromatography (HPLC) analysis. To determine the velocity of NFV efflux from LCL cells, these patients' LCL cells were incubated at 37°C in a medium containing 10 μM NFV for 3 h. The cells were then quickly washed twice with 10 ml ice-cold phosphate-buffered saline and cultured in 10 ml NFV-free medium for up to 3 h. After an interval, aliquot cells were harvested by centrifugation at 1500 ×*g* for 5 min at 4°C and immediately frozen at –80°C until HPLC analysis.

Reverse transcription-PCR (RT-PCR)

For quantification of *MDR1* transcript, RNA from 1×10^7 LCL cells was isolated using Trizol reagents (Invitrogen Corp, Carlsbad, Calif., USA). First strand cDNA was obtained by using ReverTra Ace (Toyobo, Osaka, Japan) with 1 μg of total RNA. cDNA was subjected to PCR. Information on primers and conditions for PCR was obtained as previously described [17]. We used human glyceraldehyde 3-phosphate dehydrogenase mRNA as a positive control.

Determination of intracellular concentration of NFV by HPLC

The patients' frozen LCL cells were extracted with 1.5 ml of ethanol. The extracts were then clarified by centrifugation at 2050 ×*g* for 10 min at 4°C. The ethanol extracts were evaporated at 30°C and dissolved in 180 μl of mobile phase, which was a mixture of phosphate buffer (containing 50 mM KH_2PO_4 and 50 mM Na_2HPO_4; pH 5.63) and acetonitrile (1:1, v:v) [18]. The amounts of NFV were measured using a Sensyu Pack ODS C_{18} column (5 μm particle size; 150×4.6 mm, Sensyu Scientific Co, Tokyo, Japan) at a flow rate of 1.5 ml/min by HPLC (Shimadzu Co, Tokyo, Japan). The UV detection wave length was 220 nm and efavirenz (EFV) was used as an internal standard. The lower limits of detection and quantification were 20 ng (30.1 pmole)/10^6 cells, and the calibration range was 20–2000 ng (30.1–3010 pmole/10^6 cells).

Results

We typed the three SNPs at *MDR1* 1236 (exon 12), *MDR1* 2677 (exon 21) and *MDR1* 3435 (exon 26) in DNA samples from 79 HIV-positive Japanese patients

(Figure 1). We found that it was consistent with the Hardy–Weinberg principle (Tables 1 and 2). Furthermore, in all possible two-way comparisons of the three SNPs at *MDR1* 1236 (exon 12), *MDR1* 2677 (exon 21, excluding the genotypes containing G) and *MDR1* 3435 (exon 26), we found significant linkage disequilibrium between *MDR1* 2677 A (T) and *MDR1* 1236 C (T), *MDR1* 2677 A (T) and *MDR1* 3435 C (T), and *MDR1* 1236 C (T) and *MDR1* 3435 C (T), respectively.

Figure 1. Frequency of SNPs in *MDR1*

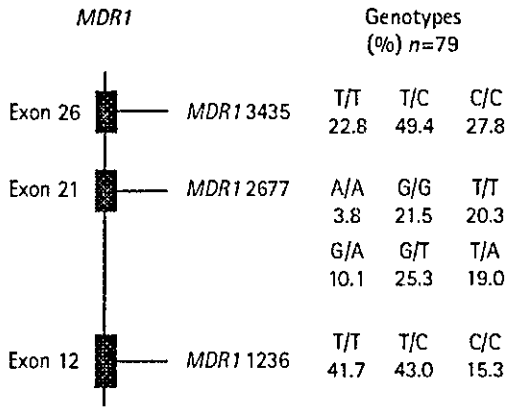

The SNPs at *MDR1* 1236, *MDR1* 2677 and *MDR1* 3435 were typed by the SNaPshot method. Genotype frequencies at each site are shown as percentage among 79 HIV-infected Japanese patients. The thin vertical line at left represents the *MDR1* gene on human chromosome 7. The closed boxes represent exons 12, 21 and 26.

Table 1. Hardy–Weinberg principle at *MDR1* 1236 (*n*=79)

	T/T	T/C	C/C
Observed number of patients	33	34	12
Expected number of patients	31.7*	36.7†	10.6‡

p: Frequency for the T allele $\frac{33\times2+34}{2\times79}=0.633$

q: Frequency for the C allele 1–p=0.367

*$79\times p^2=31.7$

†$79\times2pq=36.7$

‡$79\times q^2=10.6$

Table 2. Hardy–Weinberg principle at *MDR1* 3435 (*n*=79)

	T/T	T/C	C/C
Observed number of patients	18	39	22
Expected number of patients	17.8*	39.4†	21.8‡

p: Frequency for the T allele $\frac{18\times2+39}{2\times79}=0.475$

q: Frequency for the C allele 1–p=0.525

*$79\times p^2=17.8$

†$79\times2pq=39.4$

‡$79\times q^2=21.8$

Reportedly, *MDR1* 3435 T/T genotype was associated with lower expression of P-gp in leukocytes [13] so we hypothesized that the genotype was also associated with slower cellular export of NFV in patients' lymphocytes. To investigate this, we first established LCLs by immobilizing selected patients' PBMCs with EBV. We selected eight patients' LCLs with *MDR1* 3435 C/C (*n*=4) and T/T (*n*=4) and verified similar levels of *MDR1* in these LCLs by RT-PCR (Figure 2). We observed little variation in *MDR1* transcripts.

We found that uptake of NFV was rapid into LCLs reaching a steady-state within 5 min (Figure 3). We studied eight patients' LCLs with *MDR1* 3435 T/T and *MDR1* 3435 C/C to compare the steady-state intracellular concentration of NFV after 3 h incubation in a medium containing 10 μM NFV. The intracellular concentrations of NFV in LCLs with *MDR1* 3435 T/T and C/C genotypes were 2593 μM and 2411 μM, respectively (*n*=4), with no statistical difference. We calculated these values by hypothesizing that the LCLs are ideal spheres (10 μm diameter) and that NFV distributes uniformly in the cell.

We then compared NFV efflux from those LCLs with different genotypes at *MDR1* 3435. Before measuring export of NFV, LCLs were cultured with NFV to a saturated level. These NFV-loaded cells were transferred to NFV-free medium and cultured for 3 h with intermittent sampling of cell aliquots. We compared the efflux of NFV from the eight patients' LCLs with *MDR1* 3435 T/T and C/C (*n*=4 each), which had been verified to express *MDR1* mRNA by

Figure 2. *MDR1* mRNA expression in LCLs

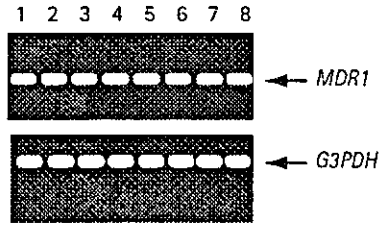

We selected eight patients' LCLs with *MDR1* 3435 C/C (lanes 1–4) and T/T (lanes 5–8) and measured the expression of *MDR1* mRNA. Total cellular RNA from LCLs was subjected to RT-PCR with primer sets for *MDR1* and *G3PDH* transcripts. Aliquots were subjected to agarose gel electrophoresis. The genotypes at *MDR1* 1236, 2677 and 3435: lanes 1 and 2, (T/T, G/G, C/C); lane 3, (T/C, G/A, C/C); lane 4 (C/C G/A C/C); lane 5 (T/T, G/T, T/T); and lanes 6–8 (T/T, T/T, T/T).

RT-PCR (Figure 2). The concentration of intracellular NFV in LCLs with the homozygous T/T genotype at *MDR1* 3435 was higher than in those with C/C genotype at 120 min and 180 min. This difference was statistically significant (P=0.04 and 0.02, respectively, Mann–Whitney U-test, Figure 4). This meant the NFV efflux in patients' LCL cells with the *MDR1* 3435 T/T genotype was slower than that with C/C genotype. Thus, we suspect the activity of P-gp in patients' LCLs with the *MDR1* 3435 T/T genotype is lower than that with the C/C genotype.

To examine the influence of *MDR1* 3435 genotypes on the response to treatment, we assessed increase in CD4 cell counts and viral suppression in 21 patients after initiation of HAART. At first, we hoped to analyse data obtained from a group of patients receiving NFV alone as a PI, but could not, due to the small number of NFV-receiving patients. Thus, we carried out the analysis in those patients receiving PIs including NFV (n=11), indinavir (n=4) and saquinavir/lopinavir/ritonavir (n=6). CD4 cell counts before treatment were similar among patients with various genotypes. Patients with various genotypes at *MDR1* 3435 showed similar changes in CD4 cell counts (Figure 5A) and viral suppression (Figure 6A) during 9 months of HAART. We found patients with the *MDR1* 1236 T/T showed higher increase in CD4 cell counts at 1 month (148 cells/μl) and 9 months (264 cells/μl) after initiation of therapy than those with *MDR1* 1236 C/C (20 cells/μl and 34 cells/μl, respectively) (Figure 5C). We suspected that *MDR1* 1236 T/T was associated with a higher rate of recovery of CD4 cell counts for patients receiving HAART with PI. We did not find differences in rates of viral suppression among the patients with various *MDR1* 1236 genotypes (Figure 6C). We did not observe a statistical difference in CD4 cell counts or viral loads among patients with different *MDR1* 2677 genotypes (Figures 5B and 6B).

Figure 3. A typical time course of NFV uptake

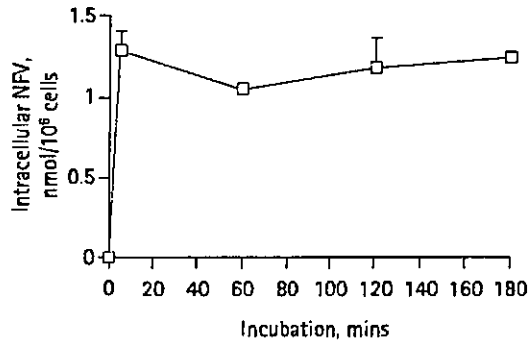

LCL cells (1 ×10⁶/10 ml) were incubated in medium containing 10 μM of NFV. Cells were harvested at 0, 5, 60, 120 and 180 min and assayed for intracellular NFV by HPLC. The horizontal axis shows the incubation time in min. The vertical axis shows the intracellular amount of NFV per 10⁶ cells. The error bars represent the standard deviations.

Figure 4. NFV efflux from patients' LCLs

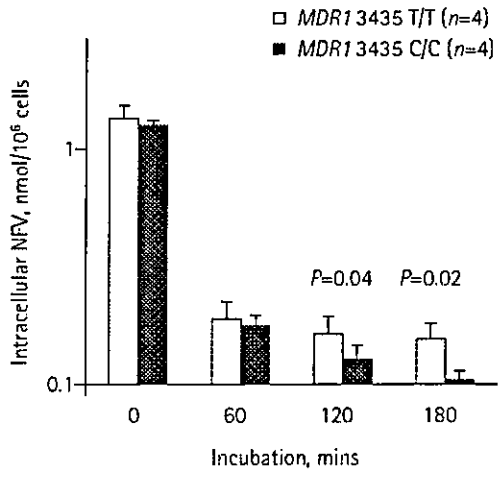

LCL cells were incubated in medium containing 10 μM of NFV for 3 h. Cells were then washed and cultured in NFV-free medium. Intracellular concentration of NFV was determined at 0, 60, 120 and 180 min by HPLC. The horizontal axis shows the incubation time in min. The vertical axis shows the intracellular amount of NFV per 10⁶ cells. We selected eight patients (described in the legend to Figure 2) and examined the velocity of NFV efflux from those cells. The intracellular concentration of NFV was measured several times in all patients' LCLs, and data were similar in every test. The error bars represent the standard deviations.

Discussion

In this study, we genotyped three SNPs at *MDR1* 1236 (exon 12), *MDR1* 2677 (exon 21) and *MDR1* 3435 (exon 26) (Figure 1) in 79 HIV-positive Japanese patients and found incomplete linkage disequilibrium – as has also been reported in other ethnic groups [6]. We found that genotype frequencies of the SNPs at *MDR1* 1236 (exon 12) and *MDR1* 3435 (exon 26) in this population were in Hardy–Weinberg equilibrium. This suggested that the studied population was precisely genotyped and unbiased in terms of the *MDR1* gene. We compared the activity of P-gp among patients' LCLs with different *MDR1* 3435 genotypes by measuring NFV efflux from the cultured LCL cells by HPLC. We found that the intracellular concentration of NFV in LCLs with the homozygous T/T genotype at *MDR1* 3435 was higher than in those with the C/C genotype at 120 min and 180 min. This difference was statistically significant (P=0.04 and 0.02, respectively; Mann–Whitney U-test; Figure 4). In contrast, in the retrospective evaluation of 21 HIV-positive patients

Figure 5. Increase in CD4 cell count among patients with the various genotypes of *MDR1* during antiretroviral treatment

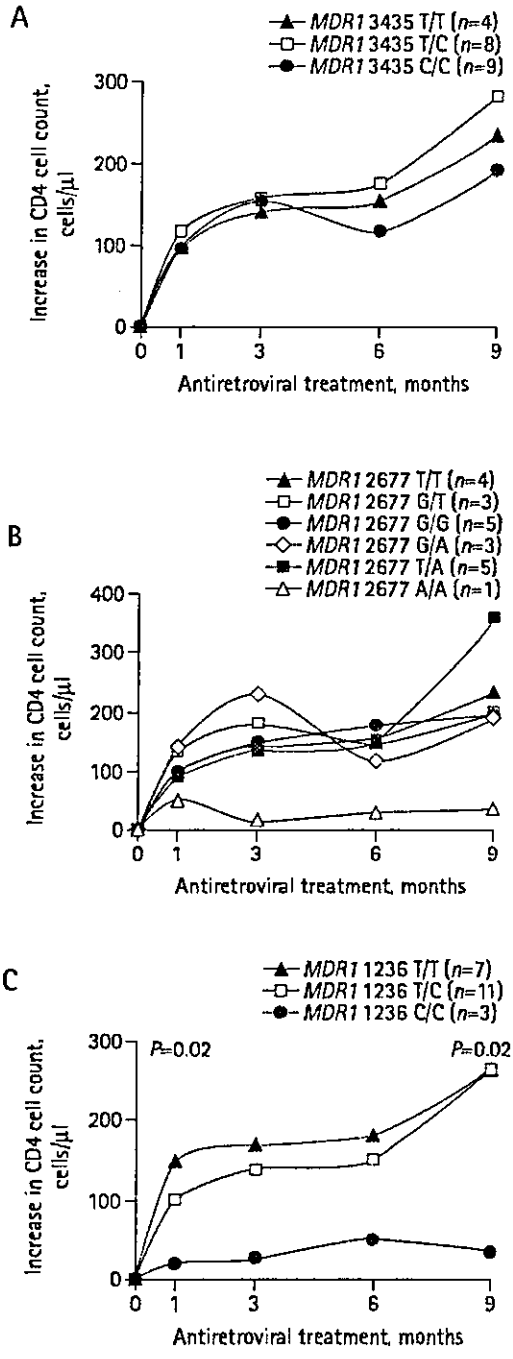

We assessed increase in CD4 cell counts among 21 patients. Every subject had CD4 cell counts and viral loads at months 0, 1, 3, 6 and 9. (A) *MDR1* 3435: T/T (▲); C/C (●); T/C (□). (B) *MDR1* 2677: T/T (▲); G/G (●); G/T (□); G/A (◇); T/A (■); A/A (△). (C) *MDR1* 1236: T/T (▲); C/C (●); T/C (□). The vertical axis shows the increase in CD4 cell count during treatment. *P* values were calculated by the Mann–Whitney U-test.

Figure 6. Suppression of viraemia among patients with various genotypes of MDR1 after antiretroviral treatment

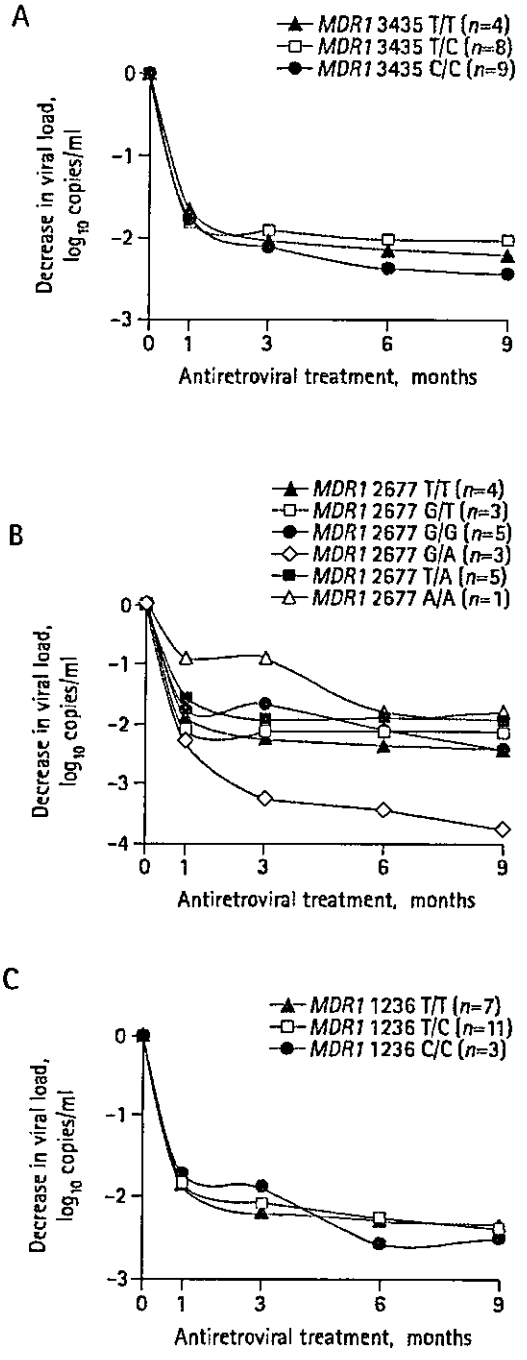

We assessed suppression of viraemia among the same 21 patients as described in the legend to Figure 5. (A) *MDR1* 3435: T/T (▲); C/C (●); T/C (□). (B) *MDR1* 2677: T/T (▲); G/G (●); G/T (□); G/A (◇); T/A (■); A/A (△). (C) *MDR1* 1236: T/T (▲); C/C (●); T/C (□). The vertical axis shows decrease in viral load. Values are shown as $\log_{10}$ copies/ml plasma.